J. Fluid Mech. (1998), *vol.* 377, *pp.* 65–97. Printed in the United Kingdom

The structure and dynamics of vorticity and rate of strain in incompressible homogeneous turbulence

By KEIKO K. NOMURA AND GARY K. POST

Department of Applied Mechanics and Engineering Sciences,
University of California at San Diego, La Jolla, CA 92093-0411, USA

(Received 23 April 1997 and in revised form 7 July 1998)

The structure and dynamics of vorticity $\boldsymbol{\omega}$ and rate of strain $\boldsymbol{S}$ are studied using direct numerical simulations (DNS) of incompressible homogeneous isotropic turbulence. In particular, characteristics of the pressure Hessian $\boldsymbol{\Pi}$, which describe non-local interaction of $\boldsymbol{\omega}$ and $\boldsymbol{S}$, are presented. Conditional Lagrangian statistics which distinguish high-amplitude events in both space and time are used to investigate the physical processes associated with their evolution. The dynamics are examined on the principal strain basis which distinguishes vortex stretching and induced rotation of the principal axes of $\boldsymbol{S}$. The latter mechanism is associated with misaligned $\boldsymbol{\omega}$ with respect to $\boldsymbol{S}$, a condition which predominates in isotropic turbulence and is dynamically significant, particularly in rotation-dominated regions of the flow. Locally-induced rotation of the principal axes acts to orient $\boldsymbol{\omega}$ towards the direction of either the intermediate or most compressive principal strain. The tendency towards compressive straining of $\boldsymbol{\omega}$ is manifested at the termini of the high-amplitude tube-like structures in the flow. Non-locally-induced rotation, associated with $\boldsymbol{\Pi}$, tends to counteract the locally-induced rotation. This is due to the strong alignment between $\boldsymbol{\omega}$ and the eigenvector of $\boldsymbol{\Pi}$ corresponding to its smallest eigenvalue and is indicative of the controlling influence of the proximate structure on the dynamics. High-amplitude rotation-dominated regions deviate from Burgers vortices due to the misalignment of $\boldsymbol{\omega}$. Although high-amplitude strain-dominated regions are promoted primarily by local dynamics, the associated spatial structure is less organized and more discontinous than that of rotation-dominated regions.

1. Introduction

The physical mechanism often considered in describing the generation and subsequent dynamics of small-scale motion in three-dimensional incompressible turbulence is vortex stretching, that is, the response of the vorticity vector $\boldsymbol{\omega}$ to the rate-of-strain tensor $\boldsymbol{S}$. What is commonly neglected in these descriptions is the coupled interaction of $\boldsymbol{\omega}$ and $\boldsymbol{S}$ which involves *non-local* effects. In the last decade, there has been considerable interest in the properties of $\boldsymbol{\omega}$ and $\boldsymbol{S}$. Of particular interest are those features corresponding to high-amplitude $\boldsymbol{\omega}^2$ and $\boldsymbol{S}^2$ (where $\boldsymbol{\omega}^2 = \omega_k\omega_k$ and $\boldsymbol{S}^2 = \mathrm{tr}[S_{ij}S_{ij}]$) which are associated with small-scale-intermittency. However, this has brought about various outstanding issues which are discussed below.

The rate of strain tensor $\boldsymbol{S}$ may be described in terms of its principal eigenvalues α, β, γ, where $\alpha \geqslant \beta \geqslant \gamma$, and the corresponding eigenvectors $\boldsymbol{e}_\alpha$, $\boldsymbol{e}_\beta$, and $\boldsymbol{e}_\gamma$. In the case of constant density flow, incompressibility requires that $\alpha + \beta + \gamma = 0$. Thus,

α is always positive (extensional), γ is always negative (compressive), and β can be either positive or negative depending on the magnitudes of α and γ. An analysis of homogeneous turbulence (Betchov 1956) showed that in order to have net production of $\boldsymbol{\omega}^2$, there must be a predominance $\beta > 0$ in the flow. Statistics obtained from direct numerical simulations (DNS) of both unsheared and sheared homogeneous turbulence (Kerr 1985; Ashurst *et al.* 1987; She, Jackson & Orszag 1991; Ruetsch & Maxey 1991; Nomura & Elghobashi 1992) support this condition and show increased probability of $\beta > 0$ in regions of high-amplitude $\boldsymbol{S}^2$. An enhanced probability for $\boldsymbol{\omega}$ to orient towards $\boldsymbol{e}_\beta$ in regions of high-amplitude $\boldsymbol{\omega}^2$ and $\boldsymbol{S}^2$ is also observed in the above studies. This feature, also observed in experiment (Tsinober, Kit & Dracos 1992), appears counterintuitive regarding vortex stretching. It would seem more likely that $\boldsymbol{\omega}$ be aligned with the direction of the largest extensional strain rate, $\boldsymbol{e}_\alpha$, to have attained the high magnitude. Although this tendency might prevail for a material line element, it must be recognized that $\boldsymbol{\omega}$ is not passive. Furthermore, reported statistics are based on ensemble averages of single-point, single-time measurements and thus do not contain information concerning the associated spatial structure or the dynamical processes involved.

The preferred alignment of $\boldsymbol{\omega}$ and positivity of β are exhibited by solutions to the restricted Euler equations (Vieillefosse 1984; Cantwell 1992) in which the anisotropic component of the pressure Hessian Π_{ij} $(\partial^2 p/\partial x_i \partial x_j)$, which introduces non-local effects in the equation for S_{ij} (2.2), is neglected. This suggests that regions of high-magnitude $\boldsymbol{\omega}^2$ or $\boldsymbol{S}^2$ in homogeneous turbulence may be dynamically local (She *et al.* 1991). Various explanations of the preferred alignment of $\boldsymbol{\omega}$ have been presented (Majda 1991; She *et al.* 1991; Jimenez 1992); however, the physical description has been incomplete and details of the dynamics have not been clearly explained. What remains particularly unclear is the nature and role of non-local effects through pressure. These effects, by their nature, will be difficult to assess as they will depend on the particular features of a given flow; however, it may be possible to identify some characteristic behaviour in homogeneous turbulence. The significance of the pressure Hessian $\boldsymbol{\Pi}$ has been considered in several studies. Analysis of the Euler equations showed that $\boldsymbol{\omega}$ tends to coincide with an eigenvector of both $\boldsymbol{S}$ and $\boldsymbol{\Pi}$ at points of maximum $\boldsymbol{\omega}^2$ (Ohkitani 1993; Ohkitani & Kishiba 1995). The local nature of the vorticity–strain interaction and a possible role for $\boldsymbol{\Pi}$ were discussed by She *et al.* (1991). They suggest that the relative orientation of $\boldsymbol{S}$ may be controlled by non-local effects.

Since both $\boldsymbol{S}$ and $\boldsymbol{\Pi}$ can be expressed as weighted volume integrals, non-local effects may be dominated by intense nearby events which are associated with distinct spatial structure. Results from DNS of homogeneous isotropic turbulence show that the structure of vorticity depends on the local magnitude (She *et al.* 1991; Ruetsch & Maxey 1991). Regions of intense $\boldsymbol{\omega}^2$ concentrate into tube-like or filamentary structures, those of moderate $\boldsymbol{\omega}^2$ occur as sheet-like structures, and low-magnitude $\boldsymbol{\omega}^2$ regions exhibit no particular structure. The length of the tube-like structures appears to be of the order of the integral scale ℓ and the diameter of the order of the Kolmogorov microscale η or Taylor microscale λ (Vincent & Meneguzzi 1991; Jimenez *et al.* 1993). Experimental evidence of the existence of intense vortex filaments has also been reported (Douady, Couder & Brachet 1991; Villermaux, Sixou & Gagne 1995). It was found that the lifetime of these filaments is of the order of an eddy-turnover time ℓ/v.

The significance of these intense $\boldsymbol{\omega}^2$ events for the overall dynamics for turbulence is not clear. Results from DNS indicate that these regions occupy a small fraction of

the total volume and thus contribute to only a small portion of the total enstrophy (Jimenez *et al.* 1993). In general, correlation between *local* $\boldsymbol{\omega}$ and $\boldsymbol{S}$ is found to be weak in homogeneous unsheared turbulence (Jimenez *et al.* 1993; Pumir 1995). However, it may be possible that high-$\boldsymbol{\omega}^2$ events contribute to the overall energy dissipation in a non-local manner, either in space or time, which therefore cannot be found from single-point, single-time statistics. Consideration of the Burgers vortex tube (Burgers 1948; Sherman 1990) illustrates a flow in which the maxima of $\boldsymbol{S}^2$ and $\boldsymbol{\omega}^2$ do not coexist and the vortex-generated dissipation rates can represent a significant portion of the total energy dissipation (see § 2.4).

In this paper, we develop a more complete description of small-scale turbulence by considering the structure and dynamics of $\boldsymbol{\omega}$ and $\boldsymbol{S}$. The study will address some of the unresolved issues concerning reported $\boldsymbol{\omega}$ and $\boldsymbol{S}$ statistics and consider the role and nature of non-local effects in an incompressible homogeneous flow. DNS of decaying isotropic turbulence provide data for the analysis. Conditional Lagrangian statistics which distinguish high-amplitude events in both space and time are used to investigate the various characteristics and physical processes associated with their evolution. These events are defined according to the invariants of the local velocity gradient tensor allowing characterization of distinct structure and dynamical behaviour. In order to provide a comprehensive description, we first develop the framework for analysis and then discuss several simple models in this context in (§ 2). This includes the restricted Euler model which effectively describes local dynamics inherent in the Navier–Stokes equations (§ 2.3) and the Burgers vortex which illustrates implications of spatial structure (§ 2.4). An understanding of the characteristics associated with these model problems is essential in the analysis of DNS results presented in § 3.

2. Analysis preliminaries

2.1. *Dynamics of vorticity and rate of strain*

The small scales of a turbulent flow are characterized by the gradients of the velocity and not the velocity itself. The velocity gradient tensor $A_{ij} = u_{i,j}$ may be decomposed into the symmetric part (rate of strain, S_{ij}) and the anti-symmetric part (rate of rotation, R_{ij}, related to $\boldsymbol{\omega}$). The evolution of vorticity $\boldsymbol{\omega}$, expressed in terms of the material derivative, is given by

$$\frac{\mathrm{D}\omega_i}{\mathrm{D}t} = S_{ik}\omega_k + \nu\frac{\partial^2\omega_i}{\partial x_k \partial x_k} \tag{2.1}$$

and that of the rate-of-strain tensor S_{ij} by

$$\frac{\mathrm{D}S_{ij}}{\mathrm{D}t} = -S_{ik}S_{kj} - \tfrac{1}{4}(\omega_i\omega_j - \delta_{ij}\omega_k\omega_k) - \frac{1}{\rho}\frac{\partial^2 p}{\partial x_i \partial x_j} + \nu\frac{\partial^2 S_{ij}}{\partial x_k \partial x_k}. \tag{2.2}$$

The terms on the right-hand side of (2.1) represent stretching and turning of $\boldsymbol{\omega}$ by $\boldsymbol{S}$ and viscous diffusion. From the right-hand side of (2.2), we see that the evolution of S_{ij} involves self-interaction, effects of local vorticity, local and non-local action through the pressure field, and viscous diffusion. From here on we will use Π_{ij} to denote the pressure Hessian $\partial^2 p/\partial x_i \partial x_j$ and normalize density such that $\rho = 1$.

Since the rate of strain tensor can be described in terms of its eigenvalues and eigenvectors, it is advantageous in the analysis of vortex stretching to consider the coupled system of (2.1) and (2.2) on the basis of the principal strain eigenvectors. This has also been considered in previous work (She *et al.* 1991; Dresselhaus & Tabor

1991). The following set of equations, written in its entirety to facilitate understanding, can be derived:

$$\left.\begin{aligned}
\frac{\mathrm{D}\omega_\alpha}{\mathrm{D}t} &= \alpha\omega_\alpha + \nu\nabla^2\omega_\alpha + \omega_\beta\left(\frac{\mathrm{D}\boldsymbol{e}_\alpha}{\mathrm{D}t} - \nu\nabla^2\boldsymbol{e}_\alpha\right)\cdot\boldsymbol{e}_\beta + \omega_\gamma\left(\frac{\mathrm{D}\boldsymbol{e}_\alpha}{\mathrm{D}t} - \nu\nabla^2\boldsymbol{e}_\alpha\right)\cdot\boldsymbol{e}_\gamma,\\
\frac{\mathrm{D}\omega_\beta}{\mathrm{D}t} &= \beta\omega_\beta + \nu\nabla^2\omega_\beta + \omega_\alpha\left(\frac{\mathrm{D}\boldsymbol{e}_\beta}{\mathrm{D}t} - \nu\nabla^2\boldsymbol{e}_\beta\right)\cdot\boldsymbol{e}_\alpha + \omega_\gamma\left(\frac{\mathrm{D}\boldsymbol{e}_\beta}{\mathrm{D}t} - \nu\nabla^2\boldsymbol{e}_\beta\right)\cdot\boldsymbol{e}_\gamma,\\
\frac{\mathrm{D}\omega_\gamma}{\mathrm{D}t} &= \gamma\omega_\gamma + \nu\nabla^2\omega_\gamma + \omega_\alpha\left(\frac{\mathrm{D}\boldsymbol{e}_\gamma}{\mathrm{D}t} - \nu\nabla^2\boldsymbol{e}_\gamma\right)\cdot\boldsymbol{e}_\alpha + \omega_\beta\left(\frac{\mathrm{D}\boldsymbol{e}_\gamma}{\mathrm{D}t} - \nu\nabla^2\boldsymbol{e}_\gamma\right)\cdot\boldsymbol{e}_\beta,
\end{aligned}\right\} \tag{2.3}$$

$$\left.\begin{aligned}
\frac{\mathrm{D}\alpha}{\mathrm{D}t} &= -\alpha^2 + \tfrac{1}{4}({\omega_\beta}^2 + {\omega_\gamma}^2) - \widetilde{\Pi}_\alpha + \nu\nabla^2\alpha,\\
\frac{\mathrm{D}\beta}{\mathrm{D}t} &= -\beta^2 + \tfrac{1}{4}({\omega_\alpha}^2 + {\omega_\gamma}^2) - \widetilde{\Pi}_\beta + \nu\nabla^2\beta,\\
\frac{\mathrm{D}\gamma}{\mathrm{D}t} &= -\gamma^2 + \tfrac{1}{4}({\omega_\alpha}^2 + {\omega_\beta}^2) - \widetilde{\Pi}_\gamma + \nu\nabla^2\gamma,
\end{aligned}\right\} \tag{2.4}$$

$$\left.\begin{aligned}
\frac{\mathrm{D}\boldsymbol{e}_\alpha}{\mathrm{D}t}\cdot\boldsymbol{e}_\beta &= \frac{1}{(\alpha-\beta)}(-\tfrac{1}{4}\omega_\alpha\omega_\beta - \widetilde{\Pi}_{\alpha,\beta}) + \nu(\nabla^2\boldsymbol{e}_\alpha)\cdot\boldsymbol{e}_\beta,\\
\frac{\mathrm{D}\boldsymbol{e}_\beta}{\mathrm{D}t}\cdot\boldsymbol{e}_\gamma &= \frac{1}{(\beta-\gamma)}(-\tfrac{1}{4}\omega_\beta\omega_\gamma - \widetilde{\Pi}_{\beta,\gamma}) + \nu(\nabla^2\boldsymbol{e}_\beta)\cdot\boldsymbol{e}_\gamma,\\
\frac{\mathrm{D}\boldsymbol{e}_\gamma}{\mathrm{D}t}\cdot\boldsymbol{e}_\alpha &= \frac{1}{(\gamma-\alpha)}(-\tfrac{1}{4}\omega_\gamma\omega_\alpha - \widetilde{\Pi}_{\gamma,\alpha}) + \nu(\nabla^2\boldsymbol{e}_\gamma)\cdot\boldsymbol{e}_\alpha,
\end{aligned}\right\} \tag{2.5}$$

where $\widetilde{\boldsymbol{\Pi}} = \boldsymbol{E}^T\,\boldsymbol{\Pi}\,\boldsymbol{E}$ is the pressure Hessian in the eigenvector basis and $\boldsymbol{E}, \boldsymbol{E}^T$ are orthogonal matrices whose rows and columns, respectively, are $\boldsymbol{e}_\alpha$, $\boldsymbol{e}_\beta$, $\boldsymbol{e}_\gamma$. In general, the strain basis equations describe the evolution of the coupled system of $\boldsymbol{\omega}$ and $\boldsymbol{S}$ with respect to the three unordered eigenvalues λ_1, λ_2, λ_3. In the above equations, the λ_i are identified as α, β, γ and are therefore valid as long as the eigenvalues retain their identities. The first three equations (2.3) describe the evolution of $\boldsymbol{\omega}$ in which vortex stretching is clearly distinguished. The third and fourth terms on the right-hand side arise due to the transformation and represent changes in the vorticity components due to rotation of the principal axes. The next three equations (2.4) describe the evolution of the principal strains and the last three equations (2.5) describe rotation of the principal axes; specifically, the rate of rotation in the plane composed of two of the eigenvectors about the axis of the third. For example, $(\mathrm{D}\boldsymbol{e}_\alpha/\mathrm{D}t)\cdot\boldsymbol{e}_\beta$ is the projection of $(\mathrm{D}\boldsymbol{e}_\alpha/\mathrm{D}t)$ onto the $\boldsymbol{e}_\beta$-axes and represents the rate of rotation in the plane defined by $\boldsymbol{e}_\alpha$ and $\boldsymbol{e}_\beta$. Note that in this coupled system, positive directions on the principal axes are defined by the vorticity vector, thus, ω_α, ω_β, ω_γ are positive quantities. The sign of the terms, e.g. $-\frac{1}{4}\omega_\alpha\omega_\beta$, then indicates the sense of rotation in this coordinate system. When (2.5) is substituted into (2.3), the viscous terms in (2.5) cancel and the effective rate of rotation of the principal axes is given by, e.g.

$$\dot{\Omega}_{\boldsymbol{e}_\alpha-\boldsymbol{e}_\beta} \equiv \frac{\mathrm{D}\boldsymbol{e}_\alpha}{\mathrm{D}t}\cdot\boldsymbol{e}_\beta - \nu(\nabla^2\boldsymbol{e}_\alpha)\cdot\boldsymbol{e}_\beta = -\frac{1}{\alpha-\beta}(\tfrac{1}{4}\omega_\alpha\omega_\beta + \widetilde{\Pi}_{\alpha,\beta}). \tag{2.6}$$

Note that $\dot{\Omega}_{\boldsymbol{e}_\alpha-\boldsymbol{e}_\beta} = -\dot{\Omega}_{\boldsymbol{e}_\beta-\boldsymbol{e}_\alpha}$, i.e. $\dot{\Omega}$ is an antisymmetric tensor. The terms involving $\dot{\Omega}$ represent the transfer of vorticity components which can alter the relative orientation of $\boldsymbol{\omega}$ with respect to the principal axes. From the right-hand side of (2.6), it is clear that a rotation of the principal axes may be induced by both local (e.g. $\omega_\alpha\omega_\beta$) and non-local (e.g. $\widetilde{\Pi}_{\alpha,\beta}$) effects. She *et al.* (1991) suggest that the former is responsible for the preferential alignment of $\boldsymbol{\omega}$ and $\boldsymbol{e}_\beta$ in homogeneneous turbulence. This mechanism

is demonstrated by the restricted Euler equations (§2.3). Note that a misalignment of $\boldsymbol{\omega}$ must exist in order for this mechanism to be active and for the off-diagonal components of $\widetilde{\boldsymbol{\Pi}}$ to have dynamic significance. As a further note, a role reversal between the eigenvalues (change in identities) will occur only if $\boldsymbol{\omega}$ is aligned with an eigenvector (unless the off-diagonal components of $\widetilde{\boldsymbol{\Pi}}$ exactly negate the effect of local vorticity (2.6)). In general, we do not expect exact alignment of $\boldsymbol{\omega}$ to prevail in fully developed turbulence and thus the role reversal is not likely to represent a dominant behaviour. Equations (2.3)–(2.5) together with the constraint imposed by incompressibility describe the dynamics of $\boldsymbol{\omega}$ and $\boldsymbol{S}$ associated with a fluid particle in the flow.

2.2. *Velocity gradient tensor invariants*

Since $\boldsymbol{\omega}$ and $\boldsymbol{S}$ represent the anti-symmetric and symmetric components of the velocity gradient tensor $\boldsymbol{A}$, they will depend on the nature of the eigenvalues of $\boldsymbol{A}$ which is given by the tensor invariants. The invariants for an incompressible flow can be expressed as

$$I = -(\alpha + \beta + \gamma) = 0, \tag{2.7}$$

$$II = \tfrac{1}{2}(\boldsymbol{\omega}^2/2 - \boldsymbol{S}^2), \tag{2.8}$$

$$III = -\alpha\beta\gamma - \tfrac{1}{4}(\alpha{\omega_\alpha}^2 + \beta{\omega_\beta}^2 + \gamma{\omega_\gamma}^2). \tag{2.9}$$

Since $I = 0$, local flow conditions are represented by a point in the (II, III)-plane where complex and real solutions are separated by the zero discriminant curve (Chong, Perry & Cantwell 1990),

$$D = II^3 + \tfrac{27}{4}III^2 = 0. \tag{2.10}$$

From (2.8) it is seen that $D > 0$ ($II > 0$) essentially corresponds to rotation-dominated conditions while $D < 0$ ($II < 0$) corresponds to those that are strain dominated.

The geometry of the local flow can be characterized using topological methods which are based on critical point concepts and classify elementary flow patterns in terms of the invariants of $\boldsymbol{A}$ (Perry and Chong 1987; Chong *et al.* 1990). However, this geometry is based on a linearized description of the local flow and provides a description of streamlines associated with the local, instantaneous value of velocity derivatives. As will be shown in §2.4, pathlines corresponding to a structure such as the Burgers vortex may span several regions in the (II, III)-plane. Characteristics of the invariants of $\boldsymbol{A}$ have been studied in DNS results (Chen *et al.* 1990; Cantwell 1993; Nomura & Elghobashi 1993; Soria *et al.* 1994). Notable features observed in both unsheared and sheared turbulence (Cantwell 1993) are preferences for the topologies associated with the upper left ($II > 0$, $III < 0$) and lower right ($II < 0$, $III > 0$) quadrants in the (II, III)-plane along with the prevalence of data near the origin (see figure 6). Recall that for homogeneous flows (Betchov 1956),

$$\langle II \rangle = 0, \qquad \langle III \rangle = 0, \tag{2.11}$$

where the brackets represent averaged quantities. This implies that statistically, a prevailing condition far from the origin in the (II, III)-plane must be balanced in the opposite quadrant or a preference for the origin may predominate. As will be discussed in §2.4 and §3, the noted features suggest the presence of high-amplitude stretched vortices.

2.3. *Restricted Euler equation dynamics*

Solutions to the restricted Euler equations (from here on referred to as RE) which effectively describe the dynamics of an isolated fluid particle, become singular at a finite time and the flow asymptotically evolves toward a state in which $\boldsymbol{\omega}$ is aligned with $\boldsymbol{e}_\beta$ and β is positive (Vieillefosse 1984). The underlying assumption involved is that there is no influence from adjacent fluid particles through pressure other than to ensure incompressibility. In general, the pressure Hessian $\boldsymbol{\Pi}$ includes both local and non-local effects. These can be distinguished by decomposing $\boldsymbol{\Pi}$ into an isotropic and anisotropic component (Ohkitani & Kishiba 1995):

$$\Pi_{ij} = \frac{\partial^2 p}{\partial x_i \partial x_j} = \frac{\Delta}{3}\,\delta_{ij} + \Pi^a_{ij}, \tag{2.12}$$

where $\Delta = \Pi_{ii} = \boldsymbol{\omega}^2/2 - \boldsymbol{S}^2$, the trace of $\boldsymbol{\Pi}$. The isotropic part $\Delta/3$ acts to preserve the volume of the fluid element with no directional distinction. The anisotropic part Π^a_{ij} then represents the non-local contribution that is determined by integrating over the entire flow. In the RE equations, the anisotropic components are zero and only the isotropic part is retained. By applying the assumptions of the RE problem to (2.3)–(2.5), we obtain the following system of equations:

$$\left.\begin{aligned}
\frac{\mathrm{D}\omega_\alpha}{\mathrm{D}t} &= \alpha\omega_\alpha - \frac{1}{4}\frac{\omega_\beta\omega_\alpha}{\alpha-\beta}\,\omega_\beta - \frac{1}{4}\,\frac{\omega_\gamma\omega_\alpha}{\alpha-\gamma}\,\omega_\gamma,\\
\frac{\mathrm{D}\omega_\beta}{\mathrm{D}t} &= \beta\omega_\beta + \frac{1}{4}\frac{\omega_\alpha\omega_\beta}{\alpha-\beta}\,\omega_\alpha - \frac{1}{4}\,\frac{\omega_\gamma\omega_\beta}{\beta-\gamma}\,\omega_\gamma,\\
\frac{\mathrm{D}\omega_\gamma}{\mathrm{D}t} &= \gamma\omega_\gamma + \frac{1}{4}\frac{\omega_\alpha\omega_\gamma}{\alpha-\gamma}\,\omega_\alpha + \frac{1}{4}\,\frac{\omega_\beta\omega_\gamma}{\beta-\gamma}\,\omega_\beta,
\end{aligned}\right\} \tag{2.13}$$

$$\left.\begin{aligned}
\frac{\mathrm{D}\alpha}{\mathrm{D}t} &= -\alpha^2 + \tfrac{1}{4}({\omega_\beta}^2 + {\omega_\gamma}^2) - \frac{\Delta}{3},\\
\frac{\mathrm{D}\beta}{\mathrm{D}t} &= -\beta^2 + \tfrac{1}{4}({\omega_\alpha}^2 + {\omega_\gamma}^2) - \frac{\Delta}{3},\\
\frac{\mathrm{D}\gamma}{\mathrm{D}t} &= -\gamma^2 + \tfrac{1}{4}({\omega_\alpha}^2 + {\omega_\beta}^2) - \frac{\Delta}{3}.
\end{aligned}\right\} \tag{2.14}$$

Retained in RE dynamics are the possibilities for role reversal of the eigenvalues and locally-induced rotation of the principal axes. The latter mechanism is described by the second and third terms on the right-hand side of (2.13). Note that these terms are expressed such that the quantities are always positive and thus the preceding signs indicate the resulting effect for each vorticity component. These equations demonstrate that local $\boldsymbol{\omega}$, if misaligned with the principal axes, rotates the principal axes in such a way as to orient $\boldsymbol{\omega}$ away from the $\boldsymbol{e}_\alpha$-direction and towards that of either $\boldsymbol{e}_\beta$ or $\boldsymbol{e}_\gamma$. Once alignment is achieved, it remains since no other mechanisms exist to counteract it.

The dynamics of the RE solution are illustrated in figure 1 which gives solutions for a representative case in which $\boldsymbol{\omega}$ is initially misaligned with the strain axes. In this case, ω_α initially dominates and amplifies by vortex stretching, $\alpha\omega_\alpha$, then decreases due to the induced rotation of the axes effectively reorienting $\boldsymbol{\omega}$ towards $\boldsymbol{e}_\beta$ and, subsequently, $\boldsymbol{e}_\gamma$. Since ω_γ eventually attenuates by compressive straining, it is the component ω_β that persists. Note that the most distinct changes in the $\boldsymbol{\omega}$-components occur when two eigenvalues approach one another. This occurs, e.g., when local strain generation by ω_α causes β to increase (2.14) thereby reducing the denominator $\alpha - \beta$ and enhancing the significance of the induced rotation associated with $\omega_\alpha\omega_\beta$ (2.13).

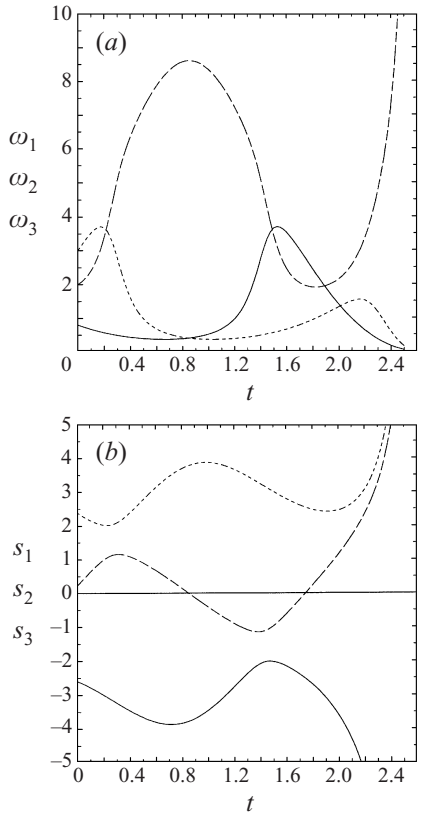

FIGURE 1. Restricted Euler solution for initially misaligned $\boldsymbol{\omega}$ ($\omega_i(0)$: 3.0 : 2.0 : 0.8; $s_i(0)$: 2.4 : 0.2 : −2.6). (*a*) $\omega_i(t)$: - - -, ω_1; – – –, ω_2; ——, ω_3; (*b*) $s_i(t)$: - - -, s_1; – – –, s_2; ——, s_3.

This effect inhibits the occurrence of a role reversal in this system of equations. In general, the coupled local dynamics of $\boldsymbol{\omega}$ and $\boldsymbol{S}$ reflect the competing effects of amplification/attenuation by stretching/compressive straining, $\boldsymbol{\omega}$-component transfer by axes rotation, and vorticity-generated strain. The alignment of $\boldsymbol{\omega}$ with $\boldsymbol{e}_\beta$ then represents a limiting configuration in the coupled system of $\boldsymbol{\omega}$ and $\boldsymbol{S}$. Note that the singular behaviour in the RE problem is due to a positive feedback established by $\Delta < 0$, which represents a source for β (2.14), and leads to an enhanced growth rate,

$$\frac{\mathrm{D}^2\omega}{\mathrm{D}t^2} = -\widetilde{\Pi}_\beta\omega = -\frac{\Delta}{3}\omega. \tag{2.15}$$

Cantwell (1992) showed that solutions to the RE equations are given by lines of constant discriminant (2.10) representing a family of curves on the (II, III)-plane. The invariants evolve along curves of constant D towards the right-hand half ($III > 0$) of the (II, III)-plane and all solutions lead to $II < 0$ ($\Delta < 0$). In all RE solutions, III eventually becomes positive. Recall the expression for III (2.9),

$$III = \underbrace{-\alpha\beta\gamma}_{III_s} + \underbrace{-\tfrac{1}{4}(\alpha{\omega_\alpha}^2 + \beta{\omega_\beta}^2 + \gamma{\omega_\gamma}^2)}_{III_{s\omega}}. \tag{2.16}$$

Thus, if $III_{s\omega} = -\frac{1}{4}(\beta{\omega_\beta}^2) < 0$, $III > 0$ implies $III_s > III_{s\omega}$; that is, production of

$\boldsymbol{S}^2$ is greater than that of $\boldsymbol{\omega}^2$. In general, the two terms III_s and $III_{s\omega}$ tend to oppose each other which may be characteristic of local dynamics.

2.4. *Burgers vortices*

Burgers vortices are exact solutions to the Navier–Stokes equations and represent flows in which a balance exists between convection, diffusion, and stretching of $\boldsymbol{\omega}$ (Burgers 1948). We consider the Burgers vortex tube, which will here be referred to as BVT, in order to illustrate implications of *spatial structure* on the characteristics of $\boldsymbol{\omega}$, $\boldsymbol{S}$, and $\boldsymbol{\Pi}$†. The steady axisymmetric flow of the BVT represents the superposition of a line vortex and axisymmetric strain. In this case, the vorticity can be expressed as a function of a non-dimensional radius $\xi = r/r_B$,

$$\omega(\xi) = Re_\Gamma\, \sigma\, \mathrm{e}^{-\xi^2}, \tag{2.17}$$

where $r_B = (4\nu/\sigma)^{1/2}$, $Re_\Gamma = \Gamma/4\pi\nu$, σ is the imposed stretching strain, and Γ is the total circulation of the vortex. Associated streamlines (and pathlines) projected on the (r,θ)-plane spiral inward and along the z-axis. Representative profiles of normalized $\boldsymbol{\omega}^2$ and $\boldsymbol{S}^2$ are given in figure 2(*a*). Note that radial profiles also indicate variation along a streamline or pathline, though they do not account for the associated times. As shown in the figure, the maxima of $\boldsymbol{\omega}^2$ and $\boldsymbol{S}^2$ do not coincide, that of the latter occurring just beyond the Burgers radius $\xi = 1$. For stronger vortices, the vortex-generated contribution of $\boldsymbol{S}^2$ dominates. Evaluation of $\boldsymbol{\Pi}$ shows that its eigenvectors, $\boldsymbol{f}_1, \boldsymbol{f}_2, \boldsymbol{f}_3$, coincide with the coordinate axes r, θ, z, respectively. The eigenvectors of $\boldsymbol{S}$ are such that $\boldsymbol{e}_3$, corresponding to the imposed strain $\lambda_3 = \sigma$, coincides with the z-axis and the other two lie in the (r,θ)-plane directed at angles of $\pm\frac{1}{4}\pi$ from the radial direction r. Radial profiles of the eigenvalues of $\boldsymbol{S}$, λ_1, λ_2, λ_3, are shown in figure 2(*b*). In this flow, $\boldsymbol{\omega}$ is always aligned with $\boldsymbol{e}_3$ although the identity of λ_3 may change; i.e. a role reversal may occur. For weak vortices, $\lambda_3 = \alpha$ (figure 2*b*). As the strength of the vortex increases, the positive strain in the orthogonal plane λ_1 approaches λ_3. For a strong vortex (not shown), the generated strain λ_1 will at some point exceed σ resulting in $\lambda_3 = \beta$ and alignment of $\boldsymbol{\omega}$ with $\boldsymbol{e}_\beta$ in regions of significant $\boldsymbol{S}^2$. Radial profiles of the eigenvalues of $\boldsymbol{\Pi}$, $\lambda_{\Pi 1}$, $\lambda_{\Pi 2}$ and $\lambda_{\Pi 3}$, are shown in figure 2(*c*). We note that the ξ-dependency in $\boldsymbol{\Pi}$ is due to the effects of centrifugal force. In the vortex core, $\boldsymbol{\omega}$ is aligned with $\boldsymbol{f}_3$ and for high Re_Γ, $\lambda_{\Pi 3}$ is nearly zero. The components of $\boldsymbol{\Pi}$ in the principal strain basis are shown in figure 2(*d*). The equality of the two components $\widetilde{\Pi}_1 = \widetilde{\Pi}_2$ reflects the axisymmetry of the problem. For higher Re_Γ, $\widetilde{\Pi}_3$ is nearly zero. As will be discussed in § 3.4, consideration of the terms in (2.4) for the BVT provide insight into the significance of $\widetilde{\boldsymbol{\Pi}}$ and the nature of $\boldsymbol{S}$ (see figure 13). The main points noted here are that in a strong vortex, the non-local component of $\widetilde{\Pi}_1$ acts to promote the positive eigenvalue λ_1 in the orthogonal plane. In a weaker vortex, non-local effects are diminished in the region of maximum $\boldsymbol{S}^2$ and promotion of the strains in the orthogonal plane are due to local effects. Thus, in the BVT, alignment of $\boldsymbol{\omega}$ and $\boldsymbol{e}_\beta$ is established through the role-reversal mechanism which results from non-local generation of strain. Characteristics of the Burgers vortex layer (BVL) have also been considered. In this flow, profiles of $\boldsymbol{\omega}^2$ and $\boldsymbol{S}^2$ coincide. Alignment of $\boldsymbol{\omega}$ with $\boldsymbol{e}_\beta$ is again a result of a role reversal which, in this case, is due to local generation of strain. We note that the eigenvalues of $\boldsymbol{\Pi}$ in the BVL are constant: $\lambda_{\Pi 1} = 0$ and $\lambda_{\Pi 2} = \lambda_{\Pi 3} = -\sigma$; thus, $\boldsymbol{f}_2 - \boldsymbol{f}_3$ forms an eigenplane (y,z) in which $\boldsymbol{\omega}$ lies.

† After completing this work, a study (Andreotti 1997) was brought to our attention which also considers characteristics of the Burgers vortex.

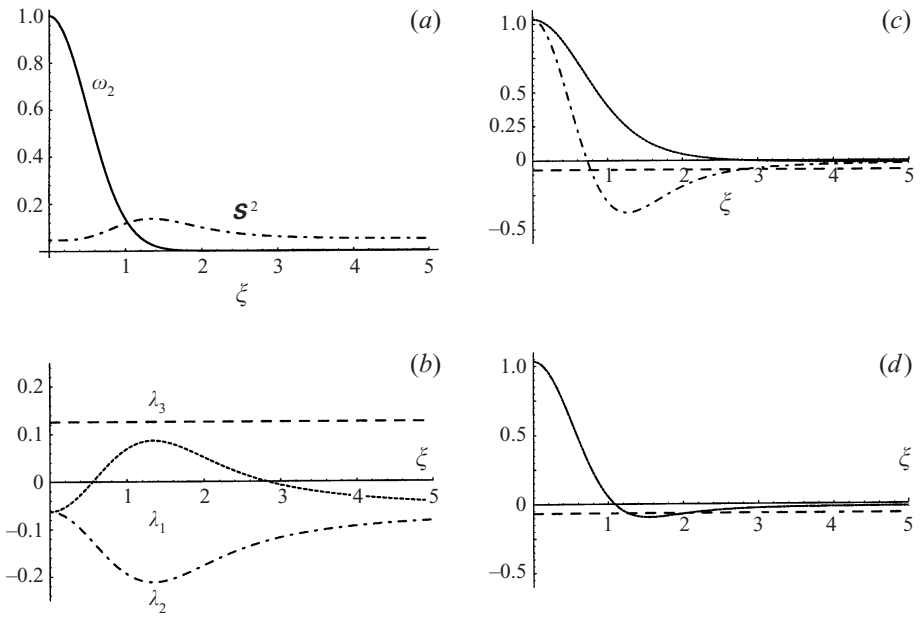

FIGURE 2. Radial profiles for BVT ($Re_\Gamma = 100/4\pi$, $\sigma = 1.0$) of (*a*) $\boldsymbol{\omega}^{2^*} = \boldsymbol{\omega}^2/\boldsymbol{\omega}_o^2$ (——) and $\boldsymbol{S}^{2^*} = \boldsymbol{S}^2/(\boldsymbol{\omega}_o^2/2)$ (– - –); (*b*) eigenvalues of S_{ij}, $\lambda_i{}^* = \lambda_i/\omega_o$ (- - - , λ_1; – – –, λ_2; – – –, λ_3); (*c*) eigenvalues of Π_{ij}, $\lambda^*_{\Pi i} = \lambda_{\Pi i}/|II_o|$ (– - –, $\lambda^*_{\Pi 1}$; ——, $\lambda^*_{\Pi 2}$; – –, $\lambda^*_{\Pi 3}$); (*d*) diagonal elements of $\widetilde{\Pi}_{ij}$, $\widetilde{\boldsymbol{\Pi}}^* = \widetilde{\boldsymbol{\Pi}}/|II_o|$ (– - –, $\widetilde{\Pi}^*_1$; - - -, $\widetilde{\Pi}^*_2$; – –, $\widetilde{\Pi}^*_3$).

Pathlines of the BVT appear as straight lines on the (II, III)-plane as shown in figure 3. Included in these figures is the $D = 0$ curve (2.10). At large r, a fluid particle exhibits $II < 0$, $III < 0$, and $D \to 0$ (lower left quadrant) which correspond to the pure axisymmetric strain at infinity. In the case of strong vortices, as a particle travels towards the centre of the vortex, the invariants first develop downwards towards the lower right quadrant ($II < 0, III > 0$) and then back upwards into the upper left quadrant ($II > 0, III < 0$). A trajectory reaching the $D = 0$ curve for $III > 0$ implies a role reversal between the positive eigenvalues. The highest point on the trajectory corresponds to conditions when the particle travels along the vortex centreline ($\xi = 0$), i.e. $II_{max} = \frac{1}{2}((Re_\Gamma\,\sigma)^2/2 - 3\sigma^2/2)$. Note that in figure 3(*a*), II and III are scaled with respect to the given BVT with $II_o = \omega_o^2/4 = (Re_\Gamma\sigma)^2/4$ and $III_o = II_o^{3/2}$ and the plots are then invariant with respect to the imposed strain σ. The effect of increasing Re_Γ is an increase in steepness of the line. In figure 3(*b*), II and III are scaled with respect to a reference BVT, in this case that of $Re_\Gamma = 100/4\pi$, $\sigma = 1$. An increase in σ is now associated with a decrease in steepness and increase in length. The effect of increasing Re_Γ (not shown) is an increase in the length of the line while maintaining the same slope. A collection of BVT trajectories for a range of Re_Γ and σ (or r_B) values would therefore generate a fan-shaped bundle of superimposed lines on the (II, III)-plane (scaled with, e.g., the ensemble average BVT). This possibility is considered in the analysis of DNS results in the next section. We note that the BVL corresponds to a point on the negative II-axis. In this case, the invariants are constant with $II < 0$, as indicated by the trace of $\boldsymbol{\Pi}$, and $III = 0$, which results from the exact counterbalance of the two quantities III_s and $III_{s\omega}$ in (2.16).

An unsteady BVT can also be considered in which the effective radius $r_\tau(t)$ is a

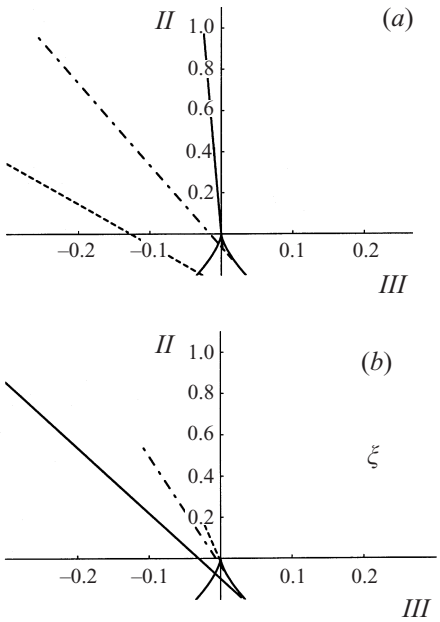

FIGURE 3. Invariant plots for steady BVT (*a*) II/II_o vs. $III/III_o(II_o = \omega_o^2/4,\ III_o = {II_o}^{3/2})$: ——, $Re_\Gamma = 1000/4\pi$; – – –, $Re_\Gamma = 100/4\pi$; - - - -, $Re_\Gamma = 50/4\pi$ ($\sigma = 1.0$ in all cases); and (*b*) $II/II_{\sigma=1}$ vs. $III/III_{\sigma=1}$: ——, $\sigma = 1.25$; – – –, $\sigma = 0.75$; - - - -, $\sigma = 0.5$ ($Re_\Gamma = 100/4\pi$ in all cases).

function of time (Sherman 1990)

$$r_\tau^2(t) = r_B^2 + (r_\tau^2(0) - r_B^2)\exp(-\tfrac{1}{2}\sigma\, t) \tag{2.18}$$

and the steady-state asymptotic solution is obtained at $t = \infty$. As indicated in (2.18), the imposed strain σ establishes the time scale for the problem. Figure 4 shows invariant characteristics along streamlines at various times for two cases of the unsteady BVT: one in which the initial effective radius is larger than the asymptotic Burgers radius ($r_\tau(0) > r_B$; figure 4*a*) and the other in which it is smaller ($r_\tau(0) < r_B$; figure 4*b*). In the former case, $\boldsymbol{\omega}^2$ is initially weak and increases in time due to stretching until $r_\tau(0) = r_B$ and equillibrium is attained. Profiles in the (II, III)-plane (normalized by II_o and III_o corresponding to the asymptotic BVT solution) exhibit a constant slope (σ constant) and increasing length (figure 4*a*). In the case where $r_\tau(0) < r_B$, $\boldsymbol{\omega}^2$ is initially stronger than the asymptotic solution and decays in time due to viscous diffusion until $r_\tau(0) = r_B$. The profiles in the (II, III)-plane show decreasing lengths in time (figure 4*b*). In either case, the lines retain a constant slope and the Lagrangian trajectories will exhibit corresponding behaviour. It must be noted that although BVT dynamics include non-local and viscous effects, the mechanism of induced rotation of the principal axes is not present since $\boldsymbol{\omega}$ is always aligned with an eigenvector of $\boldsymbol{S}$.

3. Direct numerical simulations

The RE model effectively isolates and describes the *local dynamics* of $\boldsymbol{\omega}$ and $\boldsymbol{S}$ while the BVT and BVL describe implications of *spatial structure*. We now consider Navier–Stokes turbulence where both local and non-local dynamics are present and interaction of structures occurs. DNS of homogeneous isotropic (unforced) turbulence

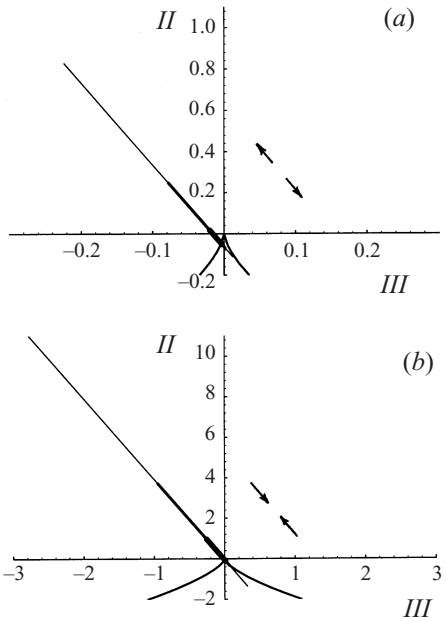

FIGURE 4. Invariant plots II/II_o vs. III/III_o for the unsteady BVT with $Re_\Gamma = 100/4\pi$, $\sigma = 1.0$: (*a*) $r_t(0)/r_B = 3.4$ ($t = 2.5$: thickest, $t = 5$: thick, $t = 10$: thin) and (*b*) $r_t(0)/r_B = 0.45$ ($t = 0.1$: thin, $t = 1.0$: thick, $t = 10.0$: thickest). Invariants scaled with corresponding steady-state BVT conditions II_o, III_o.

was performed for the analysis. The computational domain is a cube with 128^3 grid points. The simulations are initialized with a divergence-free velocity field having random fluctuations prescribed by the following energy spectrum function $E(k,0)$:

$$E(k,0) = (3\,v_o^2/2)\,(k/k_p^2)\,\mathrm{e}^{-(k/k_p)}, \tag{3.1}$$

where k_p is the wavenumber of the spectrum peak and v_o is the initial root-mean-square velocity. This spectrum function is associated with the initial period of decay for isotropic turbulence (Schumann & Patterson 1978). The initial value of k_p used here is $6(2\pi)$. The characteristic length scales of the flow are the integral length, Taylor microscale, and the Kolmogorov microscale, respectively,

$$\ell = \frac{1}{2v^2}\int \frac{E(k,t)}{k}\mathrm{d}k, \qquad \lambda = (15v^2\nu/\varepsilon)^{1/2}, \qquad \eta = (\nu^3/\varepsilon)^{1/4}, \tag{3.2}$$

where v is the root-mean-square velocity, ε is the energy dissipation rate, and ν is the kinematic viscosity. The turbulent Reynolds number, $Re_\lambda = v\lambda/\nu$, in these simulations is initially 50 and decreases to approximately 25 at $t = 5.0$. The relatively low Re_λ ensures resolution of the small scales. A criterion for adequate grid resolution is $\eta k_{max} > 1$ (Eswaran & Pope 1988). The initial value of ηk_{max} is approximately 1 and increases in time since η increases in decaying turbulence; thus the resolution criterion is satisfied throughout the entire simulation. Although Re_λ values are low, statistical characteristics such as alignment probabilities of $\boldsymbol{\omega}$ are similar to those reported in higher Re_λ simulations (Jimenez *et al.* 1993; Vincent & Meneguzzi 1994). The numerical solution scheme is based on a finite-difference method using Adams–Bashforth time integration. Details of the computational scheme are provided in (Gerz, Schumann & Elghobashi 1989; Nomura & Elghobashi 1992).

From the computed flow field, $\boldsymbol{S}$ and $\boldsymbol{\omega}$ are evaluated from the spatial derivatives of the instantaneous velocity at each grid point and at each time. From $\boldsymbol{S}$, the three principal eigenvalues ($\alpha \geqslant \beta \geqslant \gamma$) and corresponding eigenvectors ($\boldsymbol{e}_\alpha$, $\boldsymbol{e}_\beta$, $\boldsymbol{e}_\gamma$) are evaluated. Similarily, $\boldsymbol{\Pi}$ is evaluated and the principal eigenvalues ($\phi_1 \geqslant \phi_2 \geqslant \phi_3$) are determined along with their corresponding eigenvectors, $\boldsymbol{f}_1$, $\boldsymbol{f}_2$, $\boldsymbol{f}_3$. Ensemble (spatial) averaged quantities will be denoted by brackets $\langle\,\rangle$.

3.1. *Development from Gaussian initial conditions*

Although we will present statistics from DNS associated with fully developed turbulence conditions, we first remark on the development of the flow from the random initial conditions since we are interested in the inherent dynamics of the Navier–Stokes equations. Recall that the skewness of the velocity derivative, $\mathscr{S}_u$, is a measure of the nonlinear energy transfer through wavenumbers. Initially, $\mathscr{S}_u$ is zero corresponding to Gaussian (uncorrelated) conditions with no energy transfer and increases toward its asymptotic value within one eddy turnover, ℓ/v. Beyond the initial peak in $\mathscr{S}_u$, the turbulence field is regarded as fully developed. It is during this initial time period that the positivity of β and preferred alignment of $\boldsymbol{\omega}$ with $\boldsymbol{e}_\beta$ are established. As discussed, positive $\langle\beta\rangle$ must hold in developed homogeneous turbulence since $\mathscr{S}_u$ is proportional to $\langle-\alpha\beta\gamma\rangle$ (Betchov 1956). The value of $\langle\beta\rangle$ corresponding to the initial random conditions is zero and then establishes a positive value corresponding to the development in $\mathscr{S}_u$ (and the energy transfer process). A peak in $\langle\beta\rangle$ (figure 10) occurs at approximately $t = 0.4$ which corresponds to the initial peak in $\mathscr{S}_u$. Regarding the orientation of $\boldsymbol{\omega}$ with respect to the principal axes of $\boldsymbol{S}$, no preferential alignment is exhibited in the random initial conditions. As the flow develops, a predominance of ω_α is first established (figure 11) but then quickly gives way to ω_β. This occurs within the time $t = 0.4$. By $t = 1$, the preference for alignment with $\boldsymbol{e}_\beta$ is established and probability distributions of the alignment of $\boldsymbol{\omega}$ (not shown) become essentially invariant. Time scales in this flow are indicated in figure 5 which gives the development of the characteristc large-scale strain v/ℓ and small-scale strain $v/\eta^2 = (\varepsilon/v)^{1/2}$. In the fully developed flow, the development of $\langle\beta\rangle$ and $\langle\alpha\rangle$ follows closely that of v/ℓ and v/η^2, respectively. This is consistent with β being associated with $\mathscr{S}_u$ which has been shown to be essentially a large-scale quantity (She, Jackson & Orszag 1988). In general, full assessment of the time scales cannot be made here due to the limited Reynolds numbers of the simulation.

The distinctive features exhibited in the (II, III)-plane are developed along with the correlated behaviour of $\boldsymbol{\omega}$ and $\boldsymbol{S}$. As will be discussed, these features are associated with the presence of spatial structure in the flow field. The early development of $\boldsymbol{\omega}$ and $\boldsymbol{S}$ indicates that the relative orientation of $\boldsymbol{\omega}$ is a direct consequence of the dynamics of the Navier–Stokes equations. Details of the dynamics will be discussed.

3.2. *Conditional Lagrangian statistics*

In order to carry out the study in the framework developed, it is necessary to obtain statistics following a set of fluid particles. A particle tracking scheme based on a fourth-order Hermitian interpolation for the particle velocities (Truesdell 1993) was employed in the simulations. In the results presented here, 32^3 initially uniformly distributed particles are used. Ensemble-averaged statistics associated with a subset of particles meeting a specified condition (to be discussed) at a time $t = t_c$ were obtained and are denoted by $\langle\,\rangle_c$. This basic approach has previously been considered (She *et al.* 1991). Because we are interested in small-scale phenomena, timestep and grid independence was checked to ensure sufficient resolution in both time and space.

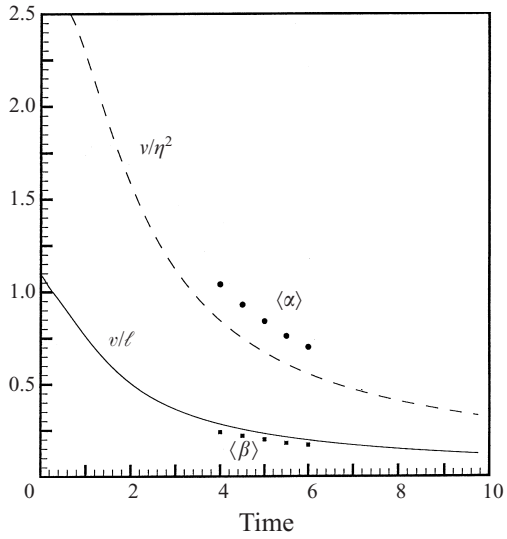

FIGURE 5. Time development of characteristic strain rates: large-scale strain v/ℓ (——), small-scale strain v/η^2 (– –), $\langle\alpha\rangle$ (circles), $\langle\beta\rangle$ (squares).

The sensitivity of the conditional statistics was also tested by varying t_c, the threshold level of the condition parameters, the total number of particles, particle injection times, and initial flow conditions (Post 1997). Although the threshold levels are arbitrary, the procedure is fairly robust and the results presented are representative of the specified conditions (see below) in terms of the qualitative features discussed.

The basis for the conditional sampling is now considered. As discussed in § 1, kinematic features and physical space structure of small-scale motion are found to depend on the magnitudes of the vorticity and rate of strain. In fact, they will depend on the relative significance of $\boldsymbol{\omega}^2$ and $\boldsymbol{S}^2$, given by II (2.8), and more generally, on both II and III. Figure 6 shows the distribution in the (II,III)-plane for the overall flow field at two times. The values of II and III are normalized by $\langle\boldsymbol{\omega}^2\rangle$ and $\langle\boldsymbol{\omega}^2\rangle^{3/2}$, respectively, for the given time. The locus of points in each distribution is essentially constant with this scaling, although it must be noted that these conditions represent a rather limited Re_λ range. The plots exhibit the previously noted preferences for the origin and upper left and lower right quadrants (the highest probability occurs near the origin). In order to interpret this distribution and determine the underlying dynamics and associated structure, we choose the (II,III)-mapping as the basis for our conditional statistics. Specifically, at a selected time $t = t_c$, we identify those particles with conditions associated with a specified region on the (II,III)-plane. Each conditional sample will be referred to by the particular quadrant (QI–QIV) of the (II,III)-plane that they reside in at $t = t_c$ (it should be understood that the particles do not necessarily retain the same topology during their evolution). Because we are interested in high-amplitude events, regions relatively far from the origin, $r_o = (II^2 + III^2)^{1/2} \geqslant 0.75$, in QII ($D_c > 0$, $III_c < 0$) and QIV ($D_c < 0$, $III_c > 0$) are selected for the conditioned samples (recall $II > 0$ implies $D > 0$). Since the frequency of occurrences are lower in QI ($D_c > 0$, $III_c > 0$) and QIII ($D_c < 0$, $III_c < 0$), the r_o threshold is lowered in these samples to 0.5 and 0.25, respectively. In addition, we consider a sample Q0 composed of regions of comparable and moderately high levels of $\boldsymbol{\omega}_c{}^2/2$ and $\boldsymbol{S}_c{}^2$ ($II_c \sim 0$, $\boldsymbol{\omega}^2 \geqslant 2\langle\boldsymbol{\omega}^2\rangle$). The particles are tracked for the duration

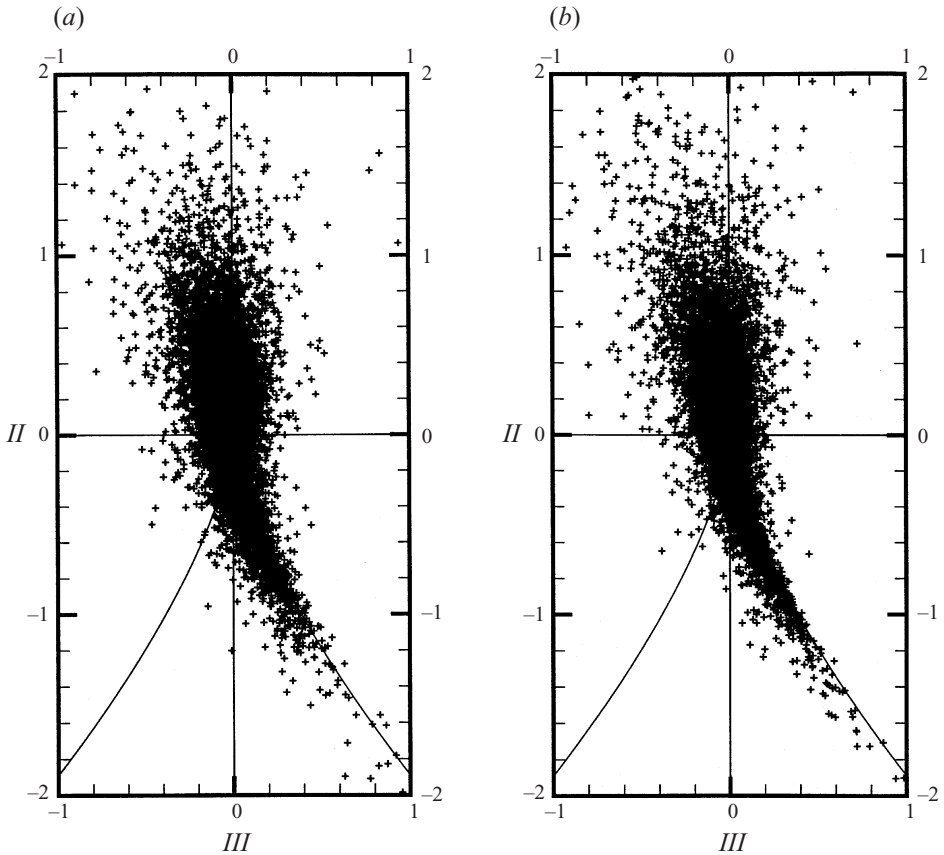

FIGURE 6. Scatter plots of normalized tensor invariants II and III (normalized by $\langle\boldsymbol{\omega}^2\rangle$ and $\langle\boldsymbol{\omega}^2\rangle^{3/2}$, respectively) for the instantaneous flow fields at (*a*) $t = 2.0$, (*b*) $t = 8.0$.

of the simulation and the resulting ensemble averages provide dynamical profiles associated with distinct small-scale motion.

3.3. *Evolution of the invariants*

The time evolution of the velocity gradient tensor invariants associated with the conditional Lagrangian samples are shown in figure 7. The plots are normalized as in figure 6. The approximate duration of the conditioned events is comparable to a representative turnover time ℓ/v during this time span. Prior to the earliest time shown in figure 7, the distributions of points tend towards that of the entire flow (figure 6). It is clear that the behaviour differs from that of the RE model; i.e. trajectories do not generally follow lines of constant D. Recall that trajectories associated with BVT structures are straight lines on the $(II - III)$-plane (figures 3 and 4). As discussed in § 2.4, a fan-shaped locus in the upper left quadrant may then indicate a collection of BVTs or similarly stretched vortices. In fact, a more distinct fan shape is observed in DNS statistics (Nomura & Elghobashi 1993) if sampling is limited to regions in the flow where $\boldsymbol{\omega}$ is essentially aligned with $\boldsymbol{e}_\beta$ thereby capturing conditions closer to the BVT configuration. If high-amplitude events are indeed associated with BVT or BVT-like structures, the QII, Q0, and QIV samples would correspond to the different regions of a structure existing at $t = t_c$ and thus represent

different age particles associated with the structures. The scaling used in the plots allows comparison with figure 3(*b*), that is, at a given time, a steep locus of points may indicate vortices with lower axial strain relative to the ensemble, or reference. Longer trajectories would indicate relatively higher Re_Γ and/or higher axial strain rate. The invariance of the flow field plots indicated in figure 6 then suggests that the collective action (and interaction) of structures yields an effective equillibrium. Individual events may correspond to behaviour as in figure 4 where an imbalance of stretching and diffusion occurs (i.e. locally non-equilibrium BVT conditions) or to non-BVT dynamics.

With these considerations, we now examine the results in figure 7 in more detail. In the case of QII (figure 7*b*), preceding t_c, we do observe an approximate fan-shaped locus of points which proceed towards the upper left quadrant. In contrast to the behaviour of a BVT, values of the invariants do not remain high in the upper left quadrant as would be expected for particles occupying a steady vortex of infinite length; instead, they drop back towards the origin with some points moving into the upper right quadrant. Those of the QIV sample (figure 7*d*), which may correspond to younger particles of the structures, show a tendency to follow a nearly straight path towards the upper left quadrant following $t = t_c$. Those of the Q0 sample (figure 7*c*) tend to develop either towards the lower right or upper left quadrant while those of the QIII sample (not shown) do not exhibit any distinct behaviour. In general, the activities of all samples for a given t_c appear to be correlated which may suggest they are associated with the same set of structures. The evolution to and from the origin generally indicates that these particles return to and originate from the background flow, although non-equilibrium effects (figure 4) are also expected to be taking place. At the same time, other particles will exhibit high amplitudes and fill in the extreme regions of the collective BVT envelope thereby maintaining the invariance exhibited in figure 6. The duration of the conditioned events, $\sim \ell/v$, corresponds to the typical residence time of the conditioned particles in the structures. Although this does not explicitly give the lifetime of a structure, it implies that these structures should persist at least for ℓ/v. As will be shown in the case of QII, the axial strain tends toward $\langle\beta\rangle_c$ which is nearly $\langle\beta\rangle$ (figure 10*b*).

The tendency for some of the particles in the QII sample to develop into the upper right quadrant is evidence of the inherent local dynamics described by the RE equations. However, since the rates of transfer to ω_γ, e.g. $\omega_\alpha\omega_\gamma/4(\alpha-\gamma)$, are comparatively less than those of the associated attenuation, $\gamma\omega_\gamma$, this tendency is not likely to prevail in high-amplitude $\boldsymbol{\omega}^2$ events. The associated dynamics of the upper right quadrant is described by the QI sample (figure 7*a*). Prior to t_c, points lie predominantly in the upper half of the (II, III)-plane suggesting older particles in the corresponding structures. As time proceeds, the fluid particles travel through the vortex core. The steeper locus is consistent with a reduced axial strain which becomes negative as development progresses into the right quadrant ($III > 0$, $III_{s\omega} = -(\alpha\omega_\alpha{}^2 + \beta\omega_\beta{}^2 + \gamma\omega_\gamma{}^2)/4 > 0$).

Figure 8 shows a three-dimensional visualization of rotation-dominated structures represented by iso-surfaces of high-amplitude positive II. As indicated, regions of $III > 0$ tend to be associated with the ends of the intense tube-like structures which is consistent with the age of these particles. A close-up of a representative structure with associated vortex lines is shown in figure 8(*b*). The vortex lines diverge due to local compressive straining as indicated by $III > 0$ which occurs at the end of the structure. Figure 9 gives corresponding visualizations of high-amplitude rotation-dominated ($II > 0$; figure 9*a*) and high-amplitude strain-dominated ($II < 0$;

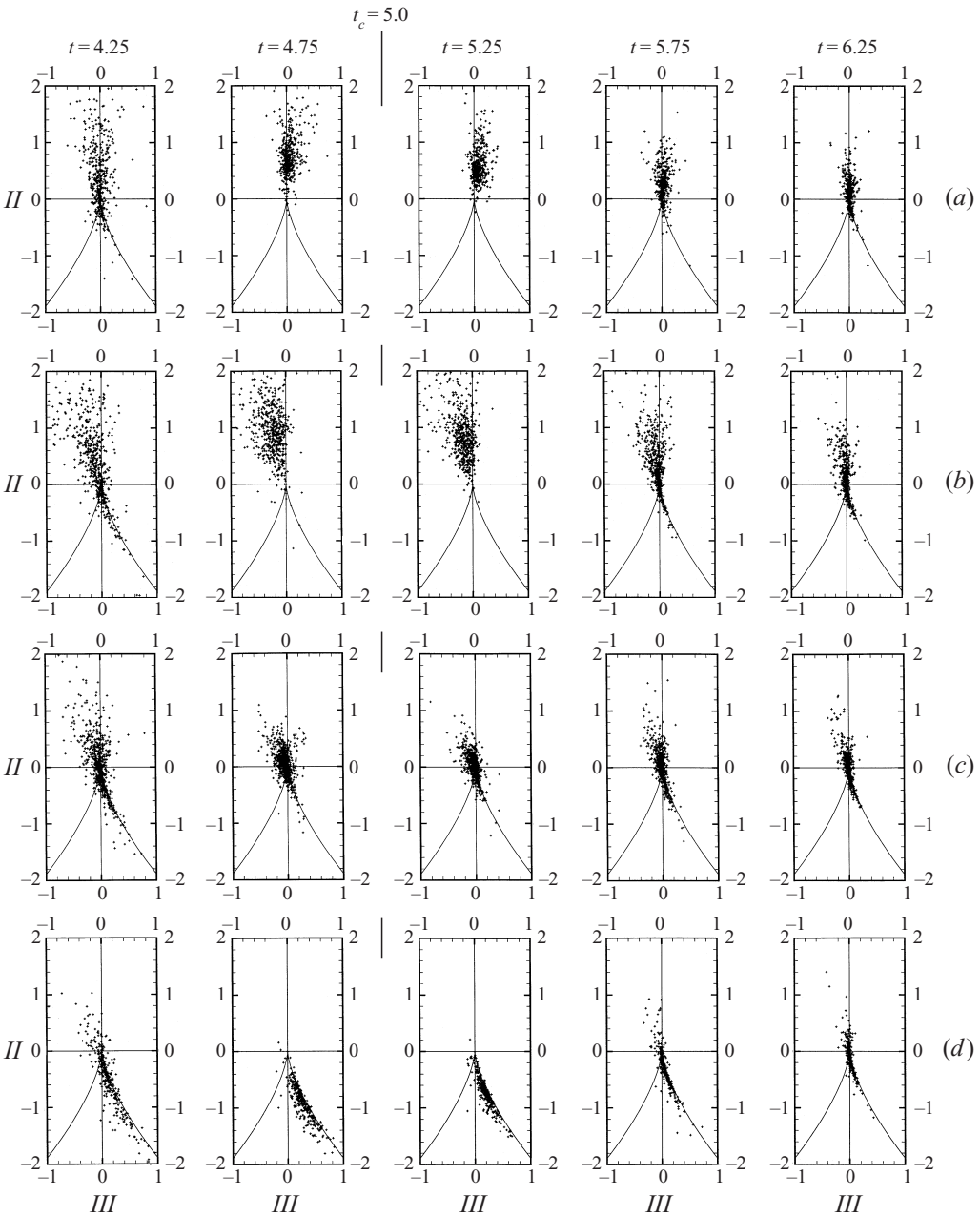

FIGURE 7. Time evolution of the normalized tensor invariants II and III for conditional Lagrangian samples with $t_c = 5.0$: (*a*) QI, (*b*) QII, (*c*) Q0, (*d*) QIV.

figure 9*b*) regions (both use same threshold magnitude of II). As indicated in these (and other visualizations not included here), negative-II structures do not coincide with the positive-II structures although they generally occur in the vicinity and some are found to surround the tubes. Strain-dominated structures are not as geometrically distinct as the rotation-dominated structures: the isoscalar surfaces are irregular and tend to be more discontinous with limited spatial extent. This may be expected since

$\boldsymbol{S}$ is associated with more complex dynamics which includes direct non-local effects (2.2). It is evident that strain-dominated regions do not simply represent the high-strain annulus of BVT structures. In general, we expect significant departure from BVT characteristics as a result of the *interaction* of structures. In order to investigate the dynamics in detail, we now examine the behaviour of $\boldsymbol{\omega}$ and $\boldsymbol{S}$.

3.4. *Dynamics of vorticity and rate of strain*

Time evolution of $\langle\omega^2\rangle_c$ and $\langle\boldsymbol{S}^2\rangle_c$ for each of the conditional samples (not shown) indicates that the general behaviour of the rotation-dominated ($II > 0$) events QII and QI are similar. The peaks in $\langle\boldsymbol{\omega}^2\rangle_c$ are preceded and followed by values of $\langle\boldsymbol{S}^2\rangle_c$ slightly above the flow field average $\langle\boldsymbol{S}^2\rangle$. In QI, the peak in $\langle\boldsymbol{\omega}^2\rangle_c$ occurs before $t = t_c$ and $\langle\boldsymbol{S}^2\rangle_c$ drops below the flow field average near $t = t_c$. In Q0, $\langle\boldsymbol{\omega}^2\rangle_c$ and $\langle\boldsymbol{S}^2\rangle_c$ evolve in parallel for the duration of the event. The behaviour of the strain-dominated ($II < 0$) events QIII and QIV are generally similar where the peaks in $\langle\boldsymbol{S}^2\rangle_c$ are preceded and followed by slightly above average $\langle\boldsymbol{\omega}^2\rangle_c$.

Differences in behaviour of the events associated with the left ($III < 0$) and right ($III > 0$) half of the (II, III)-plane are revealed in the evolution of the eigenvalues of $\boldsymbol{S}$ (figure 10). Recall the significance of the sign of III (2.16); i.e. in strain-dominated regions ($III_s > III_{s\omega}$) the sign of III indicates the sign of β while in rotation-dominated regions ($III_{s\omega} > III_s$) it indicates the straining of vorticity. For left half-plane events (QII: figure 10*a*, QIII: not shown) $< \beta >_c$ does not differ significantly from the flow field average, whereas deviations are exhibited in the right-half events (figure 10*b*, *d*). The tendency for β to approach α in QIV (figure 10*d*), and to some extent in Q0 (figure 10*c*), is also indicated in the corresponding probability distributions of the eigenvalues (not shown). This is consistent with the tendency for increased probability of positive β at high $\boldsymbol{S}^2$ (Ashurst *et al.* 1987; She *et al.* 1991) and also generally agrees with the BVT (figure 2*b*) in high-$\boldsymbol{S}^2$ regions. In the QII sample, the distribution of β (not shown) is relatively symmetric and although $\langle\beta\rangle_c$ is positive, occurrence of $\beta < 0$ is not negligible. Recall in the BVT, β is negative at the vortex centre (figure 2*b*). In QI, $\langle\beta\rangle_c$ drops below the flow field average and in fact, becomes negative (figure 10*b*).

In the evolution of the vorticity components (figure 11), we see that the predominance of ω_β is strongest in Q0. If Q0 corresponds to regions of moderately high and comparable $\boldsymbol{\omega}^2/2$ and $\boldsymbol{S}^2$ of the BVT, the tendency for ω_β should be the result of the role-reversal mechanism. As shown in figure 10(*c*), a cross-over of the two positive eigenvalues prior to t_c is not a dominant effect. From figure 7(*c*), we see that a significant portion of the Q0 sample originates from the upper left quadrant; thus, the sample includes earlier rotation-dominated events. In the case of rotation dominated conditioned events, QII (figure 11*a*) exhibits significant magnitudes of both ω_α and ω_β while QI (figure 11*b*) shows significant ω_γ. Note the sequence of occurrence in the peaks of the vorticity components in these figures: the peak in ω_α occurs first, then that of ω_β followed by ω_γ. This is consistent with RE dynamics (2.13) and shows that changes in the relative orientation of $\boldsymbol{\omega}$ and the principal axes are significant in high-$\boldsymbol{\omega}^2$ regions. The corresponding dynamics is associated with the misalignment of $\boldsymbol{\omega}$ which is not present in the BVT or BVL. In strain-dominated events, these effects will be weak due to low $\boldsymbol{\omega}^2$. Results show that ω_α dominates in QIII (not shown), while ω_β generally dominates in QIV (figure 11*d*).

Details of the dynamics of $\boldsymbol{\omega}$ are described by considering the right-hand-side terms of (2.3) in which we combine the local and non-local components of the principal

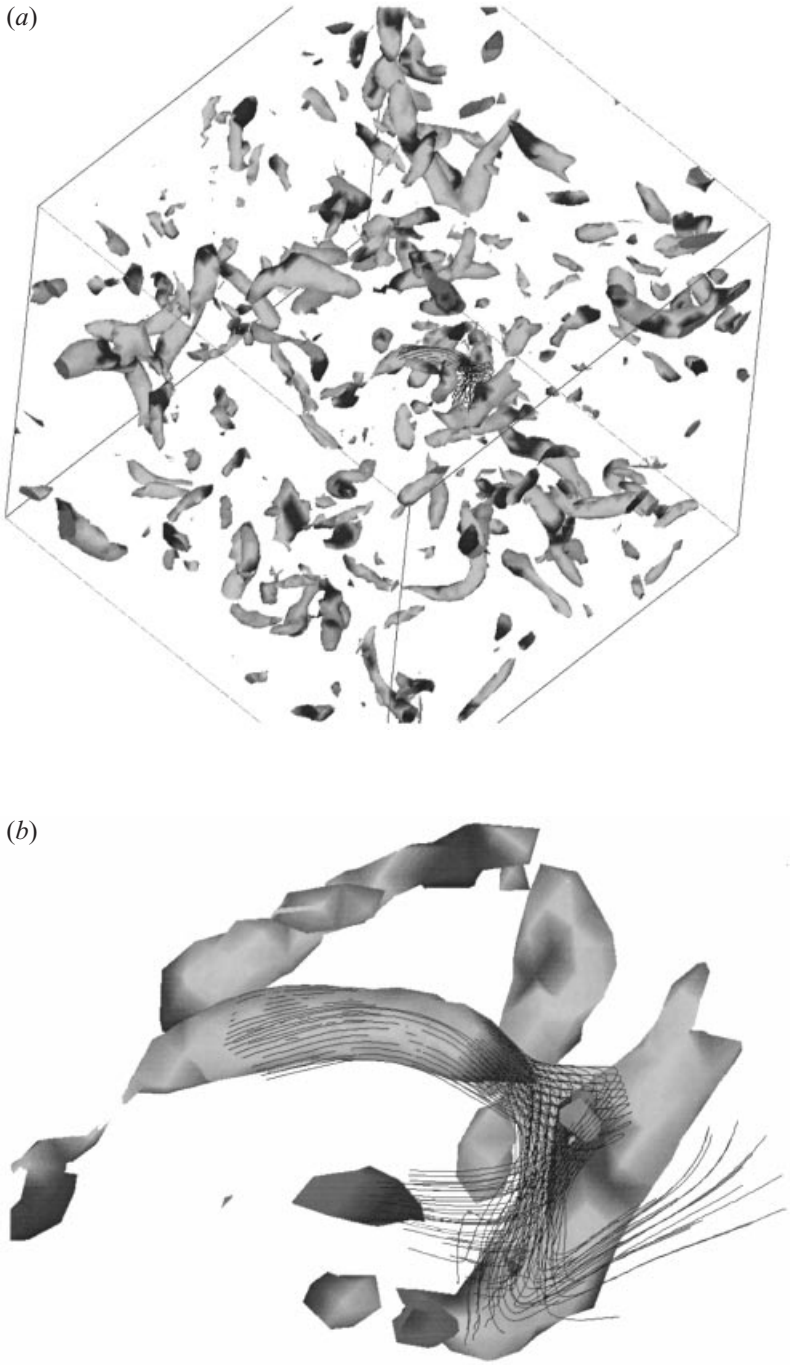

FIGURE 8. Three-dimensional visualization of rotation dominated structures represented by iso-surfaces of normalized $II = 1$ (light region: $III < 0$, dark region: $III > 0$). (*a*) 64^3 sub-domain of computational box, (*b*) closeup view of one of the structures with associated vortex lines. Note the tendency of $III > 0$, which indicates local compressive straining of vorticity, to occur at the ends of the tube-like structures.

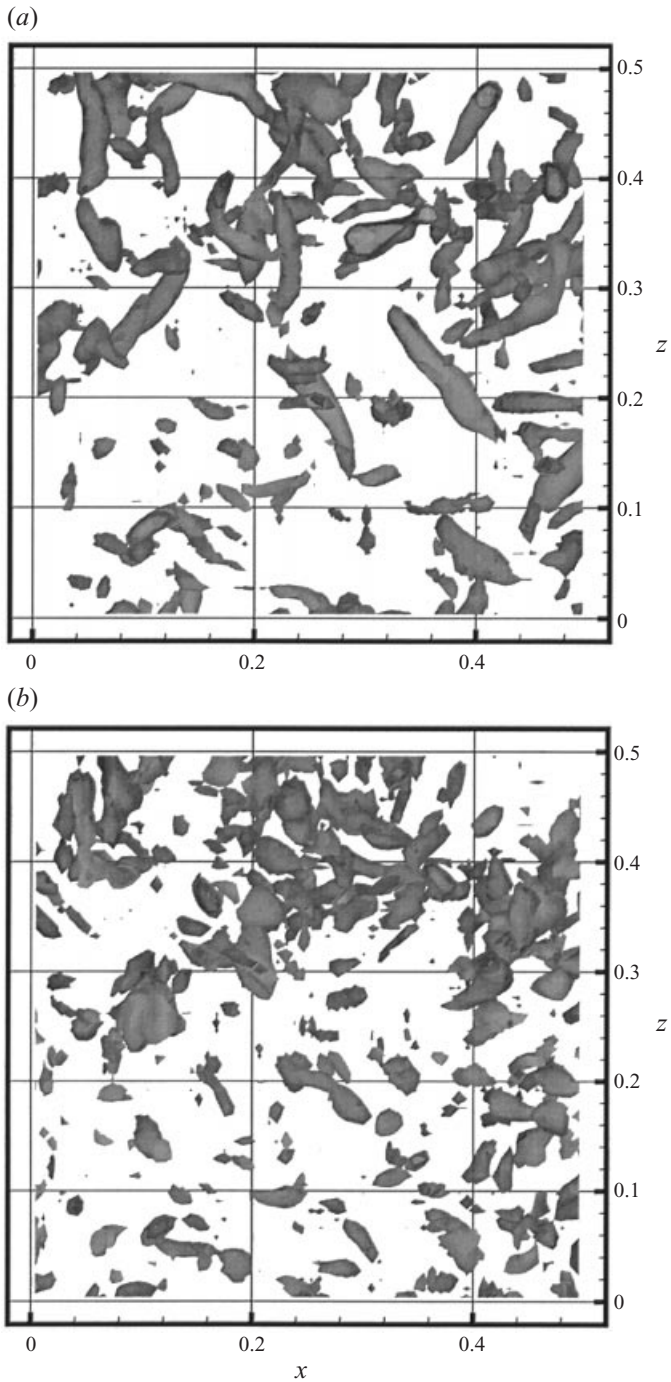

FIGURE 9. Three-dimensional visualizations ($64 \times 64 \times 32$ subdomain of computational box) of (*a*) high-amplitude rotation-dominated ($II > 0$) and (*b*) high-amplitude strain-dominated ($II < 0$) regions. Isoscalar surfaces represent the same threshold magnitude of II ($0.75\ \langle \boldsymbol{\omega}^2 \rangle$) in both cases.

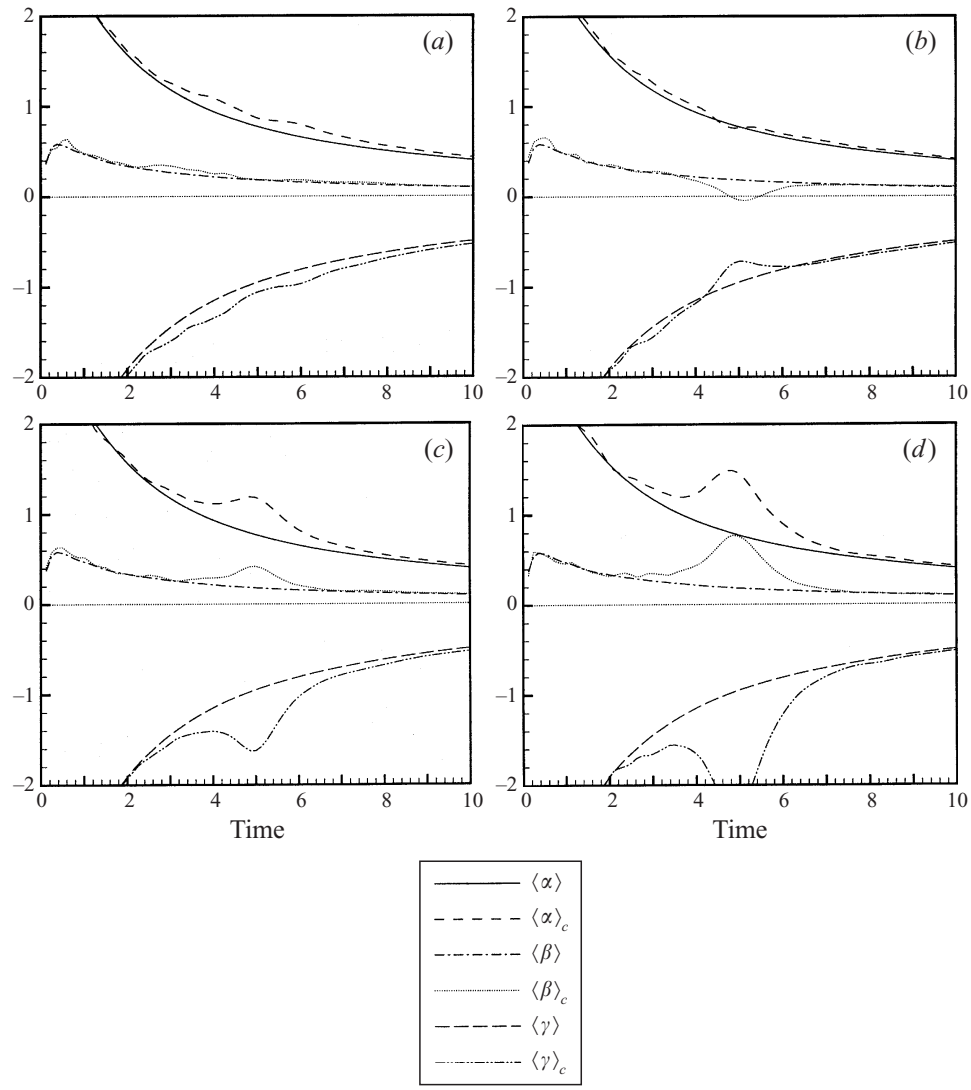

FIGURE 10. Time evolution of $\langle\alpha\rangle_c$, $\langle\beta\rangle_c$, and $\langle\gamma\rangle_c$ for conditional samples: (*a*) QII, (*b*) QI, (*c*) Q0, (*d*) QIV. Also shown are flow field average $\langle\alpha\rangle$, $\langle\beta\rangle$, and $\langle\gamma\rangle$.

axes rotation, e.g.

$$\frac{\mathrm{D}\omega_\alpha}{\mathrm{D}t} = \underbrace{\alpha\omega_\alpha}_{\text{stretch}} + \underbrace{\nu\nabla^2\omega_\alpha}_{\text{viscous}} \underbrace{-\frac{1}{4}\frac{\omega_\beta\omega_\alpha}{\alpha-\beta}\omega_\beta - \frac{1}{4}\frac{\omega_\gamma\omega_\alpha}{\alpha-\gamma}\omega_\gamma}_{\text{local}} \underbrace{-\frac{\widetilde{\Pi}_{\alpha,\beta}}{\alpha-\beta}\omega_\beta - \frac{\widetilde{\Pi}_{\alpha,\gamma}}{\alpha-\gamma}\omega_\gamma}_{\text{non-local}}. \tag{3.3}$$

The corresponding underbraced terms for each component are plotted for the conditional samples QI and QII in figure 12. Here, the viscous terms are estimated based on the evaluation of the left-hand-side term. The general behaviour for $t < 4$

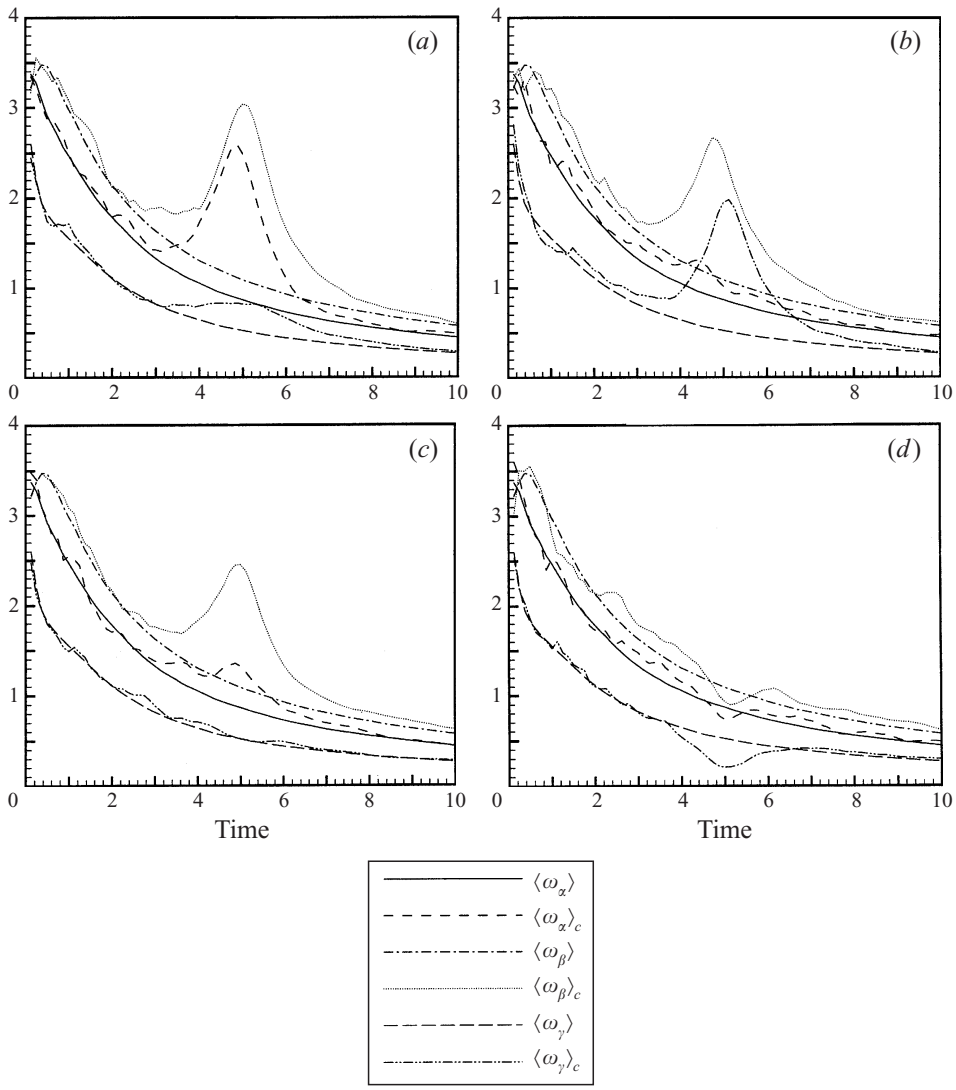

FIGURE 11. Time evolution of $\langle\omega_\alpha\rangle_c$, $\langle\omega_\beta\rangle_c$, and $\langle\omega_\gamma\rangle_c$ for conditional samples: (*a*) QII, (*b*) QI, (*c*) Q0, (*d*) QIV. Also shown are flow field average $\langle\omega_\alpha\rangle$, $\langle\omega_\beta\rangle$, and $\langle\omega_\gamma\rangle$.

follows that of the overall flow field. Total flow field results (not shown) indicate that promotion of ω_α due to vortex stretching is counterbalanced by locally-induced rotation of the principal axes which transfers ω_α to ω_β and ω_γ. Promotion of ω_β is due primarily to transfer of ω_α although there is some contribution due to vortex stretching and these are counteracted by viscous effects which are greater overall. The enhancement of ω_γ by transfer of ω_α is balanced by attenuation due to compressive straining. Non-locally-induced strain axes rotation terms are relatively small. A peak in the locally-induced rotation term in ω_β (at $t \approx 0.4$) corresponds to the peaks in $\langle\beta\rangle$ and $\langle\omega_\beta\rangle$ and indicates the significance of this mechanism in establishing fully developed conditions in the flow. In the rotation-dominated events QII and QI (figure 12), locally-induced strain axes rotation is clearly significant. Vortex stretching occurs primarily in ω_α. The transfer of ω_α to ω_β dominates in QII (figure 12*a*) whereas

the transfer of ω_α and ω_β proceeds to ω_γ in QI (figure 12*b*). In QI, a rapid change is observed in the terms for ω_β where enhancement by transfer of ω_α is converted to a loss to ω_γ. Recall that in figure 10(*b*), a negative $\langle\beta\rangle_c$ is exhibited in QI. As demonstrated by the RE solution (figure 1), a tendency of β to approach α or γ enhances the rate of induced rotation (2.5). We note that although $\langle\beta\rangle_c$ becomes negative in QI, compressive straining of $\boldsymbol{\omega}$ in this direction is not a significant factor in the dynamics. Regarding non-locally-induced rotation, this is greatest in QI and QII and is found to counteract the locally-induced rotation (figure 12). The significance of this will be discussed in § 3.5. In both QI and QII, we find viscous effects act to promote ω_α. This may be an indication of the alignment of vortex lines which occurs in the direction orthogonal to $\boldsymbol{\omega}$ and promotes the strongest filament in the vortex (Constantin, Procaccia & Segel 1995). The behaviour exhibited by Q0 and by the strain dominated events QIII and QIV (not shown) generally follow that of the overall flow.

In general, the evolution of the principal strains is more difficult to analyse. The various terms associated with the evolution of the principal eigenvalues as defined in (2.4) have been evaluated. Here, we combine local quantities and consider the anisotropic or non-local part of $\widetilde{\boldsymbol{\Pi}}$ separately, e.g.

$$\frac{\mathrm{D}\alpha}{\mathrm{D}t} = \underbrace{-\alpha^2 + \tfrac{1}{4}({\omega_\beta}^2 + {\omega_\gamma}^2) - \widetilde{\Pi}^i_\alpha}_{\text{local}} \quad \underbrace{-\widetilde{\Pi}^a_\alpha}_{\text{non-local}} \quad \underbrace{+\nu\nabla^2\alpha}_{\text{viscous}}. \tag{3.4}$$

Before considering the DNS results, we can obtain some insight by considering the behaviour of these terms in the BVT. Profiles of the corresponding underbraced terms associated with the two positive eigenvalues, λ_1 and λ_3, are shown in figure 13. In general, we see that local and non-local effects tend to counteract each other. For the imposed axial strain $\lambda_3 = \sigma$ (figure 13*b*, *d*), local and non-local effects exactly cancel as required for $\mathrm{D}\lambda_3/\mathrm{D}t = 0$. In this case, the term is positive in the rotation-dominated region ($\xi < 1$) and negative in the non-local region of significant $\boldsymbol{S}^2$. In the region of significant $\boldsymbol{S}^2$ activity ($1 < \xi < 2$), the weaker vortex (figure 13*c*) shows that promotion of λ_1 ($= \beta$) in the orthogonal plane is local and non-local effects are small. In the strong vortex (figure 13*a*), non-local $\widetilde{\Pi}^a_1$ acts to promote positive eigenvalue λ_1 ($= \alpha$). In the BVL where maxima of $\boldsymbol{\omega}^2$ and $\boldsymbol{S}^2$ coincide, strain in the orthogonal plane is promoted by local effects everywhere in the flow. In this case, the significance of non-local effects is greater for weaker vortices.

The corresponding underbraced terms for each of the eigenvalues for the DNS flow field were examined. For the total flow field (not shown), we find that non-local effects through $\widetilde{\Pi}^a_\alpha$ act to promote α. This is counteracted by local and viscous effects. In the development of β and γ, local effects represent source terms which are counteracted by viscous diffusion. The behaviour of the local and non-local terms, to some extent, resemble those of the $\boldsymbol{S}^2$ region of a strong BVT (figure 13*a*,*b*). These trends are generally observed in Q0 except that in this case local effects are enhanced and act to promote α. Results for the conditional samples QII and QIV are shown in figure 14. In QIV events where strain generation is most significant (figure 14*b*), all three eigenvalues are promoted by local effects. The trends are somewhat consistent with the high $\boldsymbol{S}^2$ region of the weaker BVT (figure 13*c*,*d*) where $\lambda_1 = \beta$ and $\lambda_3 = \alpha$. Note that in QIV, non-local effects are most significant in β and γ. As shown by figure 14(*a*), the behaviour of rotation-dominated QII events does not follow that of the corresponding region in the BVT. Rather, all three eigenvalues are promoted

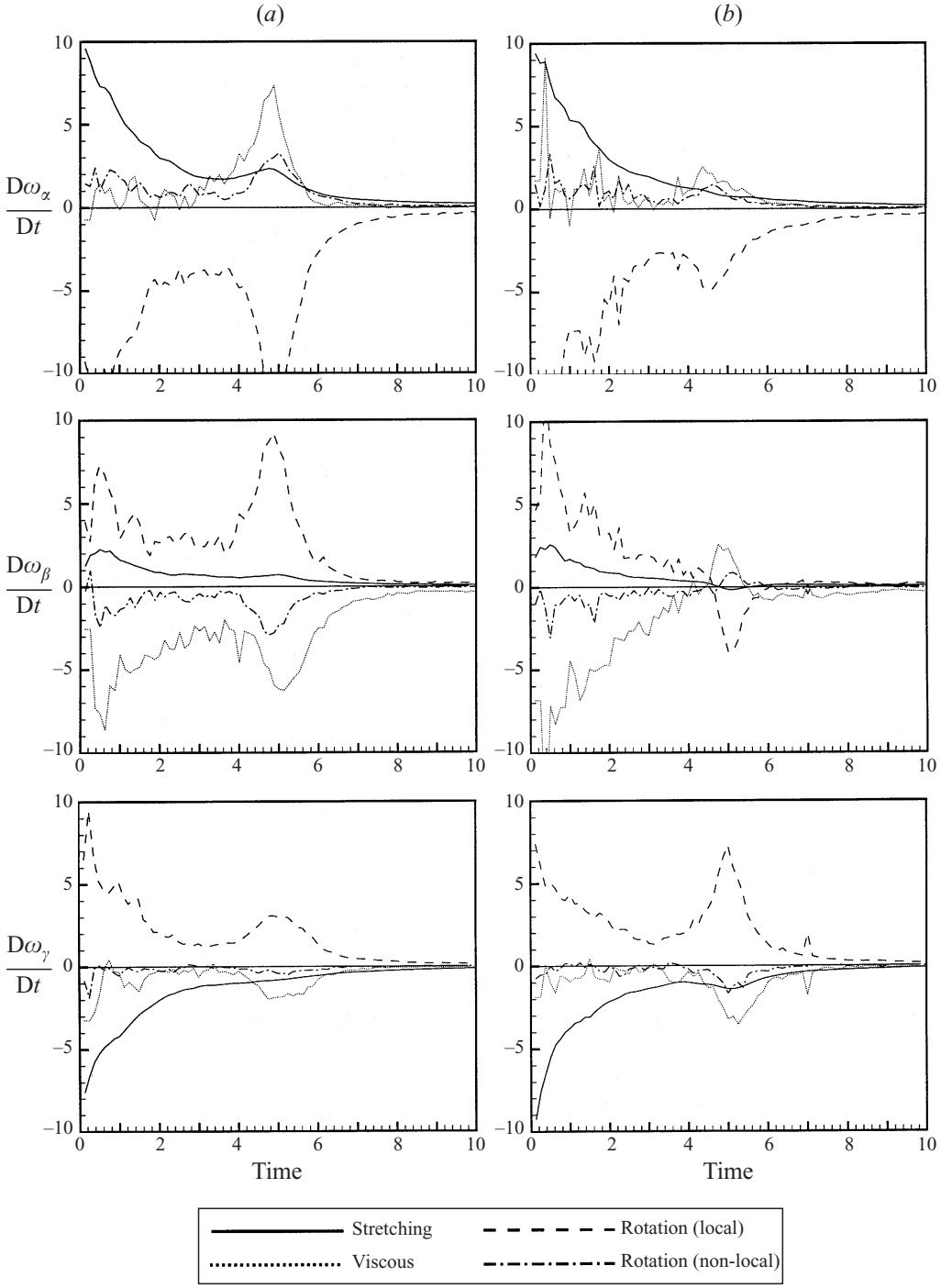

FIGURE 12. Time evolution of terms in the strain basis $\boldsymbol{\omega}$-component equations (3.3) for: (*a*) QII, (*b*) QI.

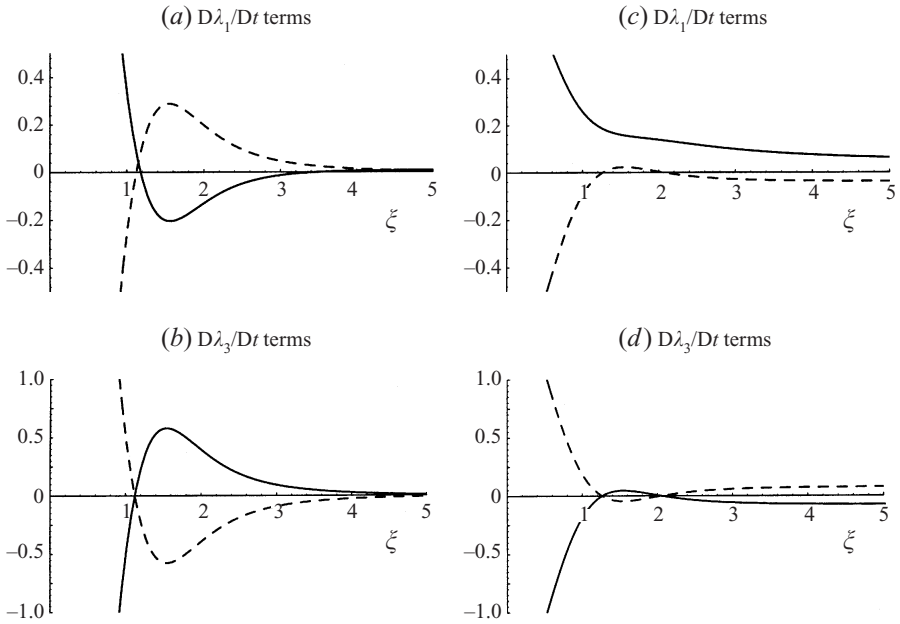

FIGURE 13. Radial profiles of the terms in the $D\lambda_i/Dt$ equation (3.4) normalized by $III_o^{2/3}$ (——, local; – –, non-local) for the BVT: (*a*,*b*) $Re_\Gamma = 1000/4\pi$, (*c*,*d*) $Re_\Gamma = 100/4\pi$ ($\sigma = 1.0$ in both cases).

by non-local effects. This may be indicative of interaction with other structures and the background flow. In the case of QI (not shown), the behaviour of $D\beta/Dt$ terms follows that of QII, however, those of $D\alpha/Dt$ and $D\gamma/Dt$ terms indicate reversing trends. This suggests that deviations from BVT behaviour are due, in part, to the changing orientation of $\boldsymbol{\omega}$ with respect to the strain axes. As will be discussed in the next section, negative values of $\widetilde{\Pi}_i^a$ are indicative of enhanced growth rates of $\boldsymbol{\omega}^2$.

3.5. *Characteristics of the pressure Hessian*

We now consider the characteristics of $\boldsymbol{\Pi}$ in more detail. In homogeneous isotropic turbulence, $\langle II \rangle = 0$ as is the trace of $\boldsymbol{\Pi}$. As expected, probability distributions (total flow) of the Π_{ij} components in the coordinate reference frame are symmetric about 0 (not shown). In contrast, probability distributions of the eigenvalues ϕ_1, ϕ_2, ϕ_3, and the strain basis components $\widetilde{\Pi}_{ij}$ are not symmetric as they reflect the structure and dynamics of $\boldsymbol{\omega}$ and $\boldsymbol{S}$. Probability distributions of ϕ_i corresponding to the conditional samples at $t = t_c$ are shown in figure 15. As expected, the distributions shift to the left or right according to II. In the rotation-dominated events QI and QII, the peaks in the distributions of ϕ_3 occur near zero. The indicated features are consistent with those of the corresponding (rotation-dominated) region in the BVT ($\xi < 1$; figure 2*c*). In particular, a high-Re_Γ BVT exhibits a value of ϕ_3 which is nearly zero although it remains negative and the other two eigenvalues ϕ_1 and ϕ_2 are positive and distinct except at the vortex centre. The behaviour of Q0 resembles that of the total flow field although the peak in the middle eigenvalue $\langle \phi_2 \rangle$ is closer to zero. As indicated in figure 2(*c*), the high strain region ($1 < \xi < 2$) of the BVT is characterized by ϕ_2 which is nearly zero and ϕ_1 and ϕ_3 of differing sign. We note that none of the conditional samples in figure 15 are consistent with the BVL or the RE model. Similarities in the features of $\boldsymbol{\Pi}$, in particular those in QII and Q0, with those of the BVT suggest similar

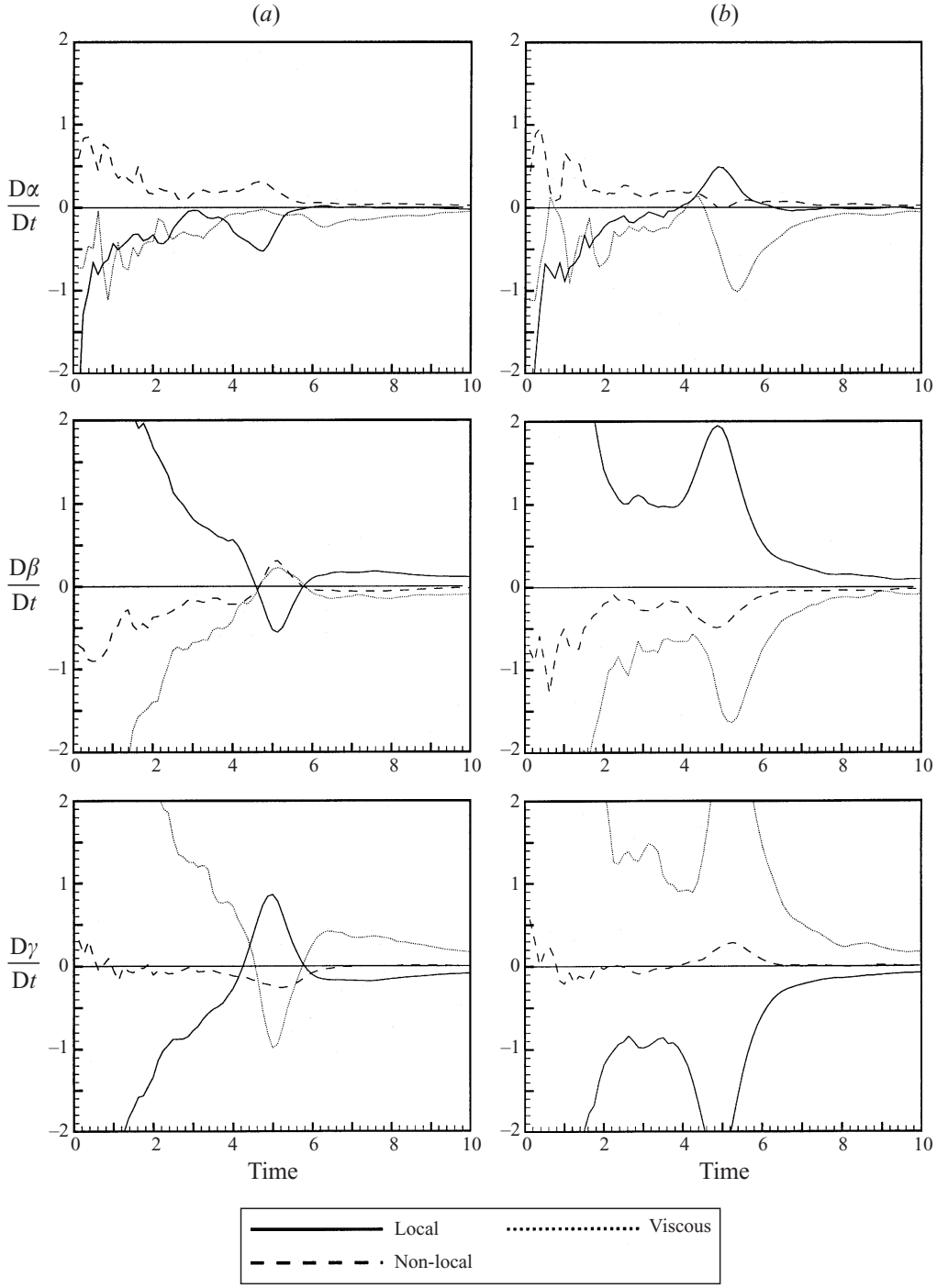

FIGURE 14. Time evolution of terms in the principal strain component equation (3.4) for: (*a*) QII, (*b*) QIV.

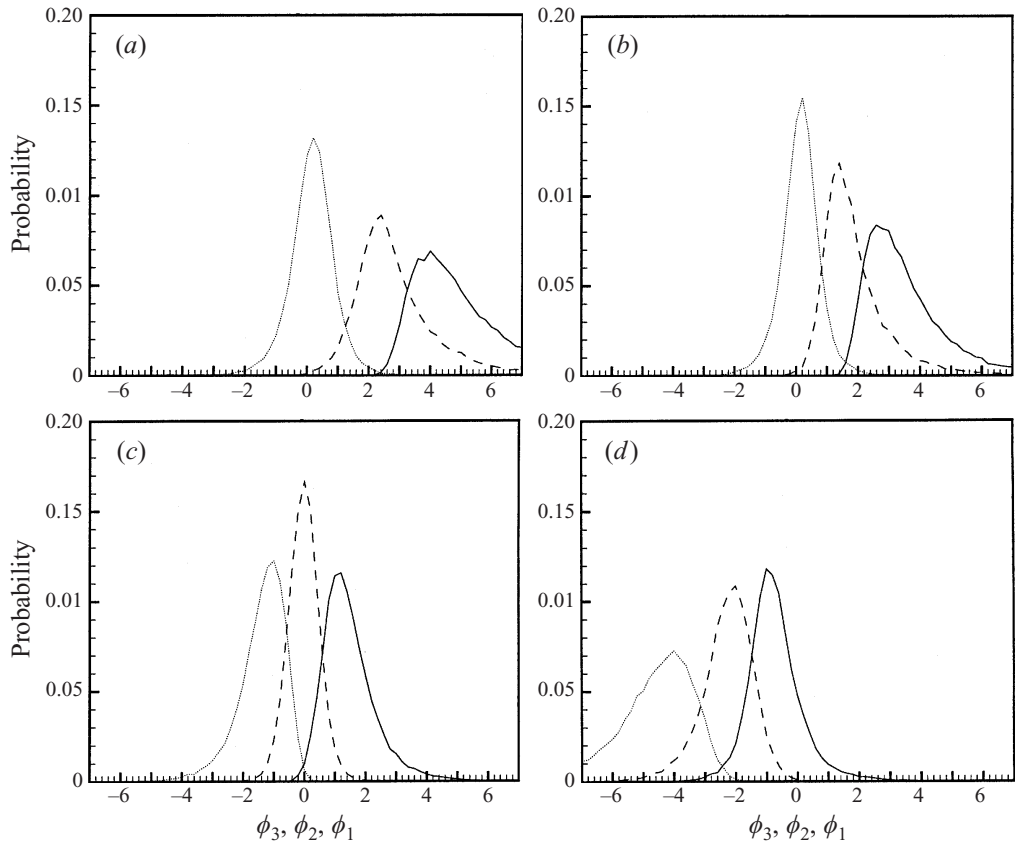

FIGURE 15. Probability distributions of $\boldsymbol{\Pi}$ eigenvalues, ϕ_1 (——), ϕ_2 (- - -), ϕ_3 (· · · · · ·), corresponding to the conditional samples at $t = t_c$: (*a*) QII, (*b*) QI, (*c*) Q0, (*d*) QIV.

spatial structure. QIV events are not consistent with any region in a BVT (except in the ambient) and must therefore be associated with other conditions present in the flow.

The dynamics associated with $\boldsymbol{\Pi}$ is established in the strain basis (2.3)–(2.5) and will thus be apparent in $\widetilde{\Pi}_{ij}$. Figure 16 shows the probability distributions of $\widetilde{\Pi}_{ij}$ for each of the conditional samples. In high-amplitude regions, the diagonal components dominate. We see the expected shift in the diagonal components to positive values for $II > 0$ and to negative values for $II < 0$. The magnitudes of the off-diagonal components of $\widetilde{\boldsymbol{\Pi}}$ are generally smaller than those of the diagonal components and tend towards negative values. They are most significant in the rotation-dominated events where in QII the leftmost peak is that of $\widetilde{\Pi}_{\alpha\beta}$ while in QI it is that of $\widetilde{\Pi}_{\beta\gamma}$. Overall, $\widetilde{\Pi}_{\alpha\beta}$ is the most prominent off-diagonal component in the flow. As discussed in § 2, the negative value implies that the associated rotation of the principal axes is in the opposite sense to that which is induced by local $\boldsymbol{\omega}$. In fact, we find that the two effects are correlated. A scatter plot of the two terms on the right-hand side of (2.6) is given in figure 17 (for QII conditions at $t = t_c$) and shows that a strong negative correlation exists between $-\widetilde{\Pi}_{\alpha\beta}/(\alpha - \beta)$ and $-\omega_\alpha\omega_\beta/4(\alpha - \beta)$.

The implication of a correlation between $\boldsymbol{\Pi}$ and $\boldsymbol{\omega}$ is indicated by (2.15), written

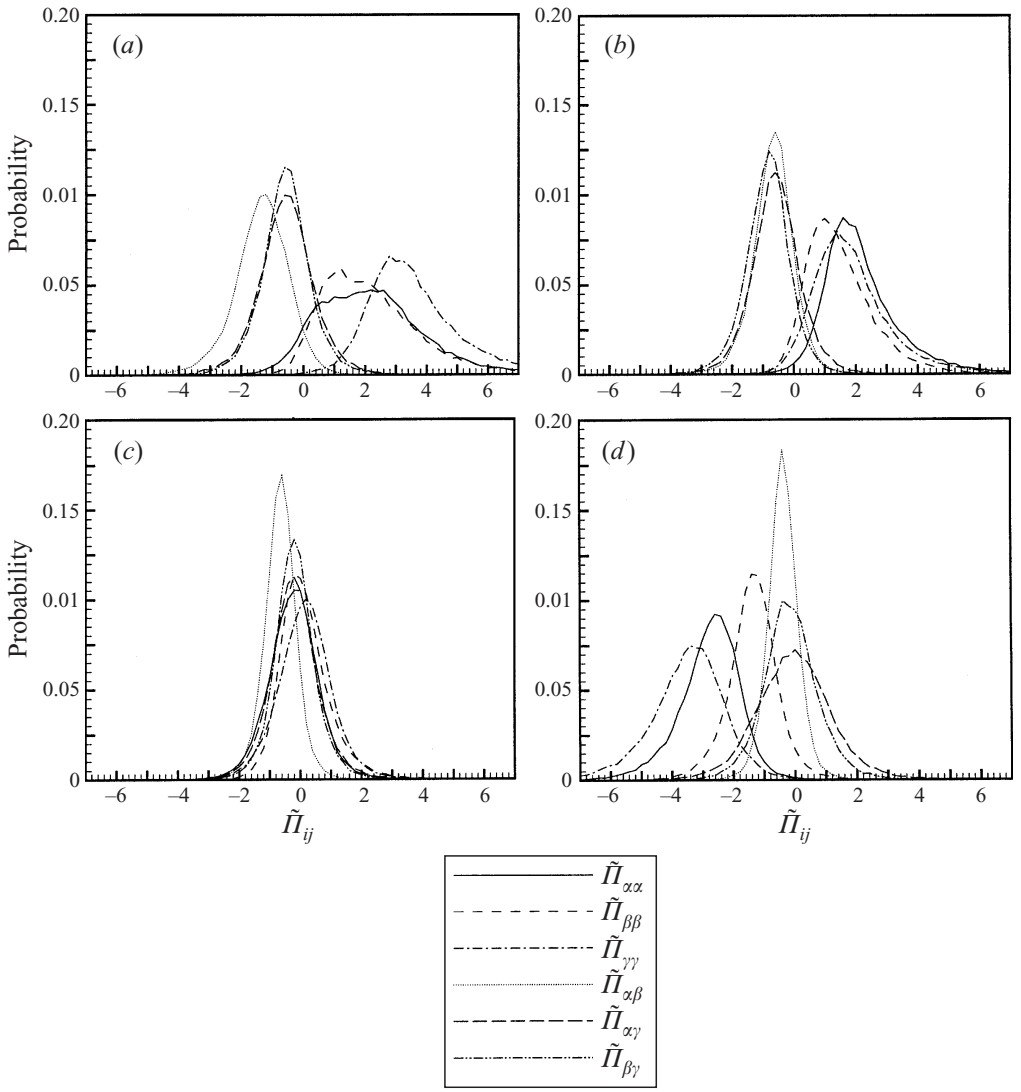

FIGURE 16. Probability distributions of the strain basis components $\widetilde{\Pi}_{ij}$ corresponding to the conditional samples at $t = t_c$: (*a*) QII, (*b*) QI, (*c*) Q0, (*d*) QIV.

here in general for an inviscid flow (Ohkitani 1993),

$$\frac{\mathrm{D}^2\omega_i}{\mathrm{D}t^2} = S_{ij}\frac{\mathrm{D}\omega_j}{\mathrm{D}t} + \frac{\mathrm{D}S_{ij}}{\mathrm{D}t}\,\omega_j = -\Pi_{ij}\omega_j, \tag{3.5}$$

i.e. it dictates the change in growth rate of ω_i. Ohkitani (1993) established for the Euler equations that if $\boldsymbol{\omega}$ of a fluid particle remains an eigenvector of $\boldsymbol{S}$, it is also an eigenvector of $\boldsymbol{\Pi}$. This implies that no rotation of the principal axes will occur, i.e. $\mathrm{D}\boldsymbol{e}_\alpha/\mathrm{D}t \cdot \boldsymbol{e}_\beta = 0$ (2.6). If $\omega = \omega_\beta$ we have

$$\frac{\mathrm{D}\omega}{\mathrm{D}t} = \beta\omega, \qquad \frac{\mathrm{D}^2\omega}{\mathrm{D}t^2} = -\phi_i\omega, \tag{3.6}$$

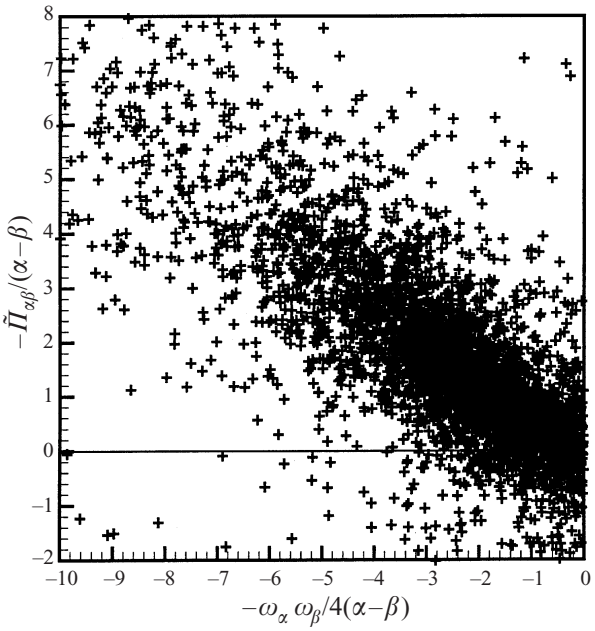

FIGURE 17. Scatter plot showing correlation between $-\widetilde{\Pi}_{\alpha\beta}/(\alpha-\beta)$ and $-\omega_\alpha\omega_\beta/4(\alpha-\beta)$. Sample consists of high-amplitude rotation-dominated ($II>0$) regions with $III<0$.

where ϕ_i is an eigenvalue of $\boldsymbol{\Pi}$. The effect of $\boldsymbol{\Pi}$ on $\boldsymbol{\omega}^2$ is given by

$$\frac{\mathrm{D}^2\frac{1}{2}\omega^2}{\mathrm{D}t^2} = (S_{ij}\omega_j)^2 - \omega_i\Pi^a_{ij}\omega_j - \frac{\Delta}{3}\omega_i^2, \tag{3.7}$$

where the decomposition of $\boldsymbol{\Pi}$ given in (2.12) is used. As noted by Ohkitani & Kishiba (1995), the isotropic part of $\boldsymbol{\Pi}$ will act to reduce growth rates of $\boldsymbol{\omega}^2$ in rotation-dominated ($\Delta>0$) regions. Thus, enhanced amplification will depend on local vortex stretching and the anisotropic part of the pressure Hessian, $\boldsymbol{\Pi}^a$. Recall that in the rotation-dominated events QII, positive strain is promoted by $\widetilde{\Pi}^a_\alpha$, $\widetilde{\Pi}^a_\beta<0$ (figure 14*a*) which thus contributes to the enhancement in growth rates of $\boldsymbol{\omega}^2$. In general, $\boldsymbol{\Pi}^a$ influences both the relative magnitudes of the principal strains and the orientation of $\boldsymbol{\omega}$ with respect to the principal strain directions (2.3)–(2.5).

Although alignment of $\boldsymbol{\omega}$ with an eigenvector of $\boldsymbol{\Pi}$ is indicated in (3.6), it is not evident from the equations which eigenvalue ϕ_i is since this is a non-local quantity. In the initial conditions of both the Taylor Green vortex (Ohkitani 1993) and the core of the BVT (§2.4), $\boldsymbol{\omega}$ aligns with the eigenvector corresponding to the smallest eigenvalue of $\boldsymbol{\Pi}$, that is, $\boldsymbol{f}_3$. This was also observed in high-$\boldsymbol{\omega}^2$ points in an Euler flow (Ohkitani & Kishiba 1995). Statistics from the present DNS results indicate a tendency for $\boldsymbol{\omega}$ to align with $\boldsymbol{f}_3$ in high-amplitude rotation-dominated events. In fact, we find that this tendency is much stronger than that associated with the alignment of $\boldsymbol{\omega}$ with $\boldsymbol{e}_\beta$ and increases as II increases. This is shown in figure 18 which gives the conditional expectation of $\cos\theta$ indicating the relative orientation of $\boldsymbol{\omega}$ with each of the eigenvectors of $\boldsymbol{S}$ and $\boldsymbol{\Pi}$ conditioned on the value of II for $III<0$ (figure 18*a*) and $III>0$ (figure 18*b*). We therefore find the coincidence of $\boldsymbol{\omega}$ and $\boldsymbol{f}_3$ to be more general than Ohkitani's conclusion for Euler dynamics; it tends to hold for strong $\boldsymbol{\omega}^2$ ($\boldsymbol{\omega}^2\gg\boldsymbol{S}^2$) regardless of the orientation of $\boldsymbol{\omega}$ with respect to the strain axes. Recall

that in the BVT, eigenvectors of $\boldsymbol{\Pi}$ coincide with the coordinate axes and $\boldsymbol{f}_3$ orients in the direction of $\boldsymbol{\omega}$. In the case of high Re_Γ, ϕ_3 is nearly zero. This is a consequence of the cylindrical geometry in which the pressure gradient is largest in the radial direction (as needed to balance the centrifugal force). Along the axis of a vortex, variation in the pressure gradient is comparatively small and values of the second derivative in this direction will be nearly zero. Since a strong vortex is characterized by $\Pi_{ii} = (\boldsymbol{\omega}^2/2 - S^2) > 0$, values orthogonal to the axis will be positive reflecting a local pressure minimum. Spatial structure is therefore significant in characterizing $\boldsymbol{\Pi}$. As observed in visualizations (e.g. figures 8, 9*a*), high-amplitude rotation dominated regions indeed exhibit tube-like structure. Since $\langle\phi_3\rangle_c$ is nearly zero, this indicates that the conditioned fluid particles are essentially travelling along the axis of these structures. The slight shift towards the positive in the distributions of figure 15(*a*, *b*) suggests a deceleration of the fluid particles. The observed correlation between the $\widetilde{\Pi}_{\alpha\beta}$ and $\omega_\alpha\omega_\beta$ terms is thus due to the concurrent tendencies for strong $\boldsymbol{\omega}$ to align with $\boldsymbol{f}_3$, which is associated with distinct spatial structure, and to orient with either $\boldsymbol{e}_\alpha$ or $\boldsymbol{e}_\beta$, which is a consequence of the inherent dynamics. This indicates that if a structure is strong enough, it will tend to control the flow in its vicinity and oppose any local changes. The dynamics will eventually affect the structure as evidenced by the tendency for $\boldsymbol{\omega}$ to become oriented along $\boldsymbol{e}_\gamma$ at the termini of the structures (figure 8). In high-amplitude strain-dominated (QIII and QIV) regions, additional statistics (Post 1997) suggest a preferential alignment of $\boldsymbol{e}_\beta$ and $\boldsymbol{f}_1$. In general, however, strong trends in the orientation between the eigenvectors of $\boldsymbol{S}$ and $\boldsymbol{\Pi}$ are not exhibited. This may be due to the absence of distinct structure in these regions (figure 9*b*).

DNS results of homogeneous sheared turbulence were also studied (Nomura, Post & Diamessis 1997; Nomura & Diamessis 1998). This flow exhibits a similar signature in the (II, III)-plane indicating the presence of stretched tube-like vortices. The fan-shape envelope in the upper left quadrant in the (II, III)-plane is relatively narrow during early stages of development indicating the dominating influence of the imposed mean strain (Nomura *et al.* 1997). During this period, the duration of high-amplitude events corresponds to the time scale of the mean rate of strain. Later in the development of the flow, the fan shape spreads out and the characteristics of the (II, III)-plane become similar to those shown here for isotropic turbulence. The coupled $\boldsymbol{\omega}$ and $\boldsymbol{S}$ dynamics and interaction with the mean flow result in the development of distinct directional features and the significance of the locally-induced rotation of the strain axes is clearly evidenced. Alignment of $\boldsymbol{\omega}$ and $\boldsymbol{f}_3$ in rotation-dominated regions is also observed. Studies of the evolution of the flow suggest that the counterbalance of locally- and non-locally-induced rotation of the principal strain axes contributes to the spatial orientation of the tube structures (Nomura & Diamessis 1998).

4. Summary and conclusions

This paper presents a physical description of small-scale turbulent motion in terms of the structure and dynamics of the vorticity vector $\boldsymbol{\omega}$ and rate-of-strain tensor $\boldsymbol{S}$. In order to effectively describe the coupled interaction of $\boldsymbol{\omega}$ and $\boldsymbol{S}$ which involves both local and non-local effects, the dynamics are examined in the principal strain basis. In this reference frame, the interaction of $\boldsymbol{\omega}$ and $\boldsymbol{S}$ through vortex stretching and through induced rotation of the principal axes of $\boldsymbol{S}$ are clearly distinguished and the dynamic significance of $\boldsymbol{\Pi}$ is established. In order to gain a physical understanding of the dynamics and to aid the interpretation of turbulence statistics,

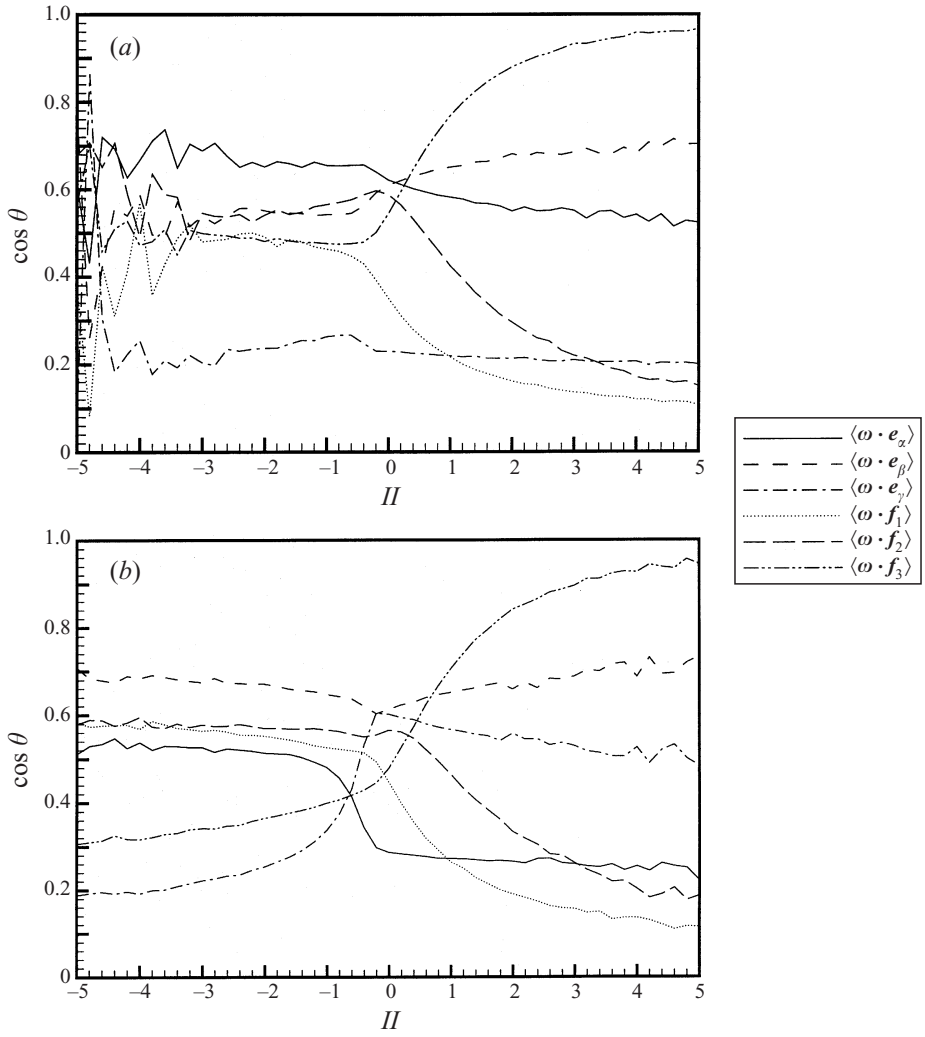

FIGURE 18. Conditional expectation of cos θ (indicating relative orientation between $\boldsymbol{\omega}$ and each of the eigenvectors of $\boldsymbol{S}$ and $\boldsymbol{\Pi}$) conditioned on the value of II for (*a*) $III < 0$, (*b*) $III > 0$.

we considered several existing models in this context. These include the restricted Euler equations (Vieillefosse 1984), which describe inviscid local dynamics inherent in the Navier–Stokes equations, and the Burgers vortices (Burgers 1948) which describe implications of spatial structure. The full dynamics occurring in homogeneous turbulence was investigated using DNS and conditional Lagrangian statistics. These statistics distinguish high-amplitude events in both space and time and reveal the physical processes associated with their evolution.

Previously reported observations in DNS of homogeneous turbulence are now clarified. Regarding the orientation of $\boldsymbol{\omega}$ with respect to the principal strain axes, this is a dynamic feature which is established through induced rotation of the principal axes by misaligned $\boldsymbol{\omega}$, a condition which predominates in homogeneous isotropic turbulence. Results show that locally-induced rotation of the principal axes is particularly significant in the dynamics of rotation-dominated regions. In general,

high-amplitude $\boldsymbol{\omega}^2$ events will be initiated through amplification along $\boldsymbol{e}_\alpha$. Locally-induced rotation of the principal axes will then act to orient $\boldsymbol{\omega}$ towards the direction of either $\boldsymbol{e}_\beta$ or $\boldsymbol{e}_\gamma$. The alignment of $\boldsymbol{\omega}$ and $\boldsymbol{e}_\beta$ is the prevailing configuration due to the dynamics of the coupled system. The tendency for $\boldsymbol{\omega}$ to orient towards the direction of $\boldsymbol{e}_\gamma$ is also observed. Since the rates associated with this process tend to be lower, we find these regions corresponding to the termini of high-amplitude rotation-dominated structures. Early development of the flow from random initial conditions demonstrates the significance of the induced strain axes rotation in establishing the energy transfer process. Statistics of the fully developed flow reflect the dynamics involved: $\boldsymbol{\omega}^2$ is generated predominantly by stretching in ω_α and attenuated by viscous action in ω_β and compressive straining in ω_γ.

In particular, we have investigated non-local aspects of the coupled dynamics of $\boldsymbol{\omega}$ and $\boldsymbol{S}$. These are described by the anisotropic component of $\boldsymbol{\Pi}$ which can modify both the amplitude and relative orientation of $\boldsymbol{S}$. As illustrated by the BVT and BVL, generation of strain is strongly influenced by spatial structure. If a vortex structure is characterized by cylindrical geometry and is strong enough, it will generate strain non-locally. Our DNS results indicate that in high-amplitude rotation-dominated events, positive strain is attributed to non-local effects whereas in strain-dominated events, local effects prevail. Non-locally-induced rotation of the principal axes through $\boldsymbol{\Pi}$ tends to counteract the locally-induced axes rotation in high-amplitude rotation-dominated regions. This is due to the strong alignment between $\boldsymbol{\omega}$ and the eigenvector $\boldsymbol{f}_3$, corresponding to the smallest (nearly zero) eigenvalue of $\boldsymbol{\Pi}$, which occurs in intense $\boldsymbol{\omega}^2$ regions and is indicative of the controlling influence of the proximate structure. If a structure is strong enough, it will dominate the flow in its vicinity and tend to oppose any local changes. Local dynamics will inevitably affect the structure as indicated by the tendency for $\boldsymbol{\omega}$ to become oriented along $\boldsymbol{e}_\gamma$ at the termini of the structures.

In summary, our results demonstrate the significance of both local RE dynamics (influence of local $\boldsymbol{\omega}$) and spatial structure (influence through non-local $\boldsymbol{\Pi}$) in the interaction of $\boldsymbol{\omega}$ and $\boldsymbol{S}$ in homogeneous turbulence. The behaviour of high-amplitude rotation-dominated events cannot be solely represented by local dynamics due to the formation of distinct spatial structure. Although the geometric structure is similar to the BVT, the associated behaviour differs due to the misalignment of $\boldsymbol{\omega}$ which may represent interaction with the surrounding flow field. High-amplitude strain-dominated regions are generated predominantly by local dynamics. The associated structure is less organized and more discontinous than that associated with rotation-dominated events. This is of particular significance since these regions will be active sites for scalar mixing and chemical reaction. Based on overall flow field averages, promotion of $\langle\alpha\rangle$ and positivity of $\langle\beta\rangle$ are associated with non-local and local effects, respectively. Non-local effects are therefore significant in the dynamics of small-scale motion. This should be considered in the interpretation of single-point statistics. Characterizations of small-scale turbulence should consider not only typical structures present but also typical structure interactions.

The first author would like to express her gratitude to Marios Fyrillas for many helpful discussions throughout the course of this work. We have also benefitted from discussions with Zhen-Su She, Javier Jiménez, Costas Pozrikidis, and Peter Diamessis. We would like to thank George Truesdell for the use of his particle tracking procedure in our DNS. We also appreciate the helpful comments provided by the Referees of our manuscript. The turbulence simulations were performed on the Cray C90 at the

San Diego Supercomputing Center (SDSC). A portion of the allocation at SDSC was provided through the University of California, San Diego. The authors are indebted to the University of California, San Diego for support for this research. A portion of this work was also funded by the National Science Foundation (CTS-9510559).

REFERENCES

Andreotti, B. 1997 Studying Burgers' models to investigate the physical meaning of the alignments statistically observed in turbulence. *Phys. Fluids* **9**, 735–742.

Ashurst, W. T., Kerstein, A. R., Kerr, R. M. & Gibson, C. H. 1987 Alignment of vorticity and scalar gradient with strain rate in simulated Navier–Stokes turbulence. *Phys. Fluids* **30**, 2343–2353.

Betchov, R. 1956 An inequality concerning the production of vorticity in isotropic turbulence. *J. Fluid Mech.* **1**, 497–504.

Burgers, J. M. 1948 A mathematical model illustrating the theory of turbulence. In *Advances in Applied Mechanics*, vol. 1, pp. 171–196. Academic.

Cantwell, B. J. 1992 Exact solution of a restricted Euler equation for the velocity gradient tensor. *Phys. Fluids* A **4**, 782–793.

Cantwell, B. J. 1993 On the behavior of velocity gradient tensor invariants in direct numerical simulations of turbulence. *Phys. Fluids* A **5**, 2008–2013.

Chen, J. H., Chong, M. S., Soria, J., Sondergaard, R., Perry, A. E., Rogers, M., Moser, R. & Cantwell, B. J. 1990 A study of the topology of dissipating motions in direct simulations of time-developing compressible and incompressible mixing layers. In *Proc. 1990 Summer Program, Center for Turbulence Research*, pp. 139–161.

Chong, M. S., Perry, A. E. & Cantwell, B. J. 1990 A general classification of three-dimensional flow fields. *Phys. Fluids* A **2**, 765–777.

Constantin, P., Procaccia, I. & Segel, D. 1995 Creation and dynamics of vortex tubes in three-dimensional turbulence. *Phys. Rev.* E **51**, 3207–3222.

Douady, S., Couder, Y. & Brachet, M. E. 1991 Direct observation of the intermittency of intense vorticity filaments in turbulence. *Phys. Rev. Lett.* **67**, 983–986.

Dresselhaus, E. & Tabor, M. 1991 The kinematics of stretching and alignment of material elements in general flow fields. *J. Fluid Mech.* **236**, 415–444.

Eswaran, V. & Pope, S. B. 1988 An examination of forcing in direct numerical simulation of turbulence. *Computers and Fluids* **16**, 257.

Gerz, T., Schumann, U. & Elghobashi, S. 1989 Direct simulation of stably stratified homogeneous turbulent shear flows. *J. Fluid Mech.* **200**, 563–594.

Jimenez, J. 1992 Kinematic alignment effects in turbulent flows. *Phys. Fluids* A **4**, 652–654.

Jimenez, J., Wray, A. A., Saffman, P. G. & Rogallo, R. S. 1993 The structure of intense vorticity in isotropic turbulence. *J. Fluid Mech.* **255**, 65–90.

Kerr, R. M. 1985 Higher-order derivative correlations and the alignment of small-scale structures in isotropic numerical turbulence. *J. Fluid Mech.* **153**, 31–58.

Majda, A. 1991 Vorticity, turbulence, and acoustics in fluid flow. *SIAM Rev.* **33**, 349–388.

Nomura, K. & Diamessis, P. 1998 The interaction of vorticity and rate of strain in turbulent homogeneous shear flow. *Phys. Fluids* (submitted).

Nomura, K. K. & Elghobashi, S. E. 1992 Mixing characteristics of an inhomogeneous scalar in isotropic and homogeneous sheared turbulence. *Phys. Fluids* **4**, 606–625.

Nomura, K. K. & Elghobashi, S. E. 1993 The structure of inhomogeneous turbulence in variable density nonpremixed flames. *Theor. Comput. Fluid Dyn.* **5**, 265–278.

Nomura, K., Post, G. & Diamessis, P. 1997 Characterization of small-scale motion in incompressible homogeneous turbulence. *AIAA Paper* 97-1956.

Ohkitani, K. 1993 Eigenvalue problems in three-dimensional Euler flows. *Phys. Fluids* A**5**, 2570–2572.

Ohkitani, K. & Kishiba, S. 1995 Nonlocal nature of vortex stretching in an inviscid fluid. *Phys. Fluids* **7**, 411–421.

Perry, A. E. & Chong, M. S. 1987 A description of eddying motions and flow patterns using critical-point concepts. *Ann. Rev. Fluid Mech.* **19**, 125–155.

Post, G. K. 1997 The dynamics of vorticity and rate-of-strain in homogeneous isotropic turbulence. M S Thesis, University of California, San Diego.

Pumir, A. 1995 A numerical study of pressure fluctuations in three-dimensional, incompressible, homogeneous, isotropic turbulence. *Phys. Fluids* **6**, 2071–2083.

Ruetsch, G. R. & Maxey, M. R. 1991 Small-scale features of vorticity and passive scalar fields in homogeneous isotropic turbulence. *Phys. Fluids* A **3**, 1587–1597.

Schumann, U. & Patterson, G. S. 1978 Numerical study of the return of axisymmetric turbulence to isotropy. *J. Fluid Mech.* **88**, 711–735.

She, Z.-S., Jackson, E. & Orszag, S. A. 1988 Scale-dependent intermittency and coherence in turbulence. *J. Sci. Comput.* **3**, 407–434.

She, Z.-S., Jackson, E. & Orszag, S. A. 1991 Structure and dynamics of homogeneous turbulence: models and simulations. *Proc. R. Soc. Lond.* A **434**, 101–124.

Sherman, F. S. 1990 *Viscous Flow*. McGraw-Hill.

Soria, J., Sondergaard, R., Cantwell, B. J., Chong, M. S. & Perry, A. E. 1994 A study of the fine-scale motions of incompressible time-developing mixing layers. *Phys. Fluids* **6**, 871–884.

Truesdell, G. C. 1993 The interaction between decaying isotropic turbulence and dispersed solid particles. PhD Dissertation, University of California, Irvine.

Tsinober, A., Kit, E. & Dracos, T. 1992 Experimental investigation of the field of velocity gradients in turbulent flows. *J. Fluid Mech.* **242**, 169–192.

Vieillefosse, P. 1984 Internal motion of a small element of fluid in an inviscid flow. *Physica* **125A**, 150–162.

Villermaux, E., Sixou, B. & Gagne, Y. 1995 Intense vortical structures in grid-generated turbulence. *Phys. Fluids* **7**, 2008–2013.

Vincent, A. & Meneguzzi, M. 1991 The spatial structure and statistical properties of homogeneous turbulence. *J. Fluid Mech.* **225**, 1–20.

Vincent, A. & Meneguzzi, M. 1994 The dynamics vorticity tubes in homogeneous turbulence. *J. Fluid Mech.* **258**, 245–254.